The Effect of Gd Substitution to the Dielectric and Optical Properties on $MnFe_{2-x}Gd_xO_4$

Dissertation submitted to the

Kerala University in partial fulfillment of requirements

for the degree of

MASTER OF SCIENCE

In

PHYSICS

University of Kerala

Project report 2020-2022

Abstract

In this work, we synthesized pristine and Gadolinium substituted $MnFe_2O_4$ and investigates their structural, electrical, and optical properties in detail. Pristine and Gd substituted spinel ferrite $MnFe_{2-x}Gd_xO_4$ (x = 0.00, 0.02, 0.04) were prepared via sol-gel method and resultant powder sintered at 500^0 C for 5 hours in a high-temperature furnace. The phase of the obtained powder is identified using the Qualx 2.24 software. From the phase identification studies, it is confirmed that $MnFe_{2-x}Gd_xO_4$ (x = 0.00, 0.02, 0.04) exhibit spinel cubic structure. X-ray diffraction (XRD) studies were performed to explain the structure of these samples and it will discuss in detail. It was observed that the lattice parameter and cell volume of $MnFe_2O_4$ increase with Gd^{3+} substitution. It is also observed that the crystalline size first decreases and then increases with Gd substitution, however, the increase is less than that of pristine $MnFe_2O_4$. The hopping length of tetrahedral and octahedral sites increases with increasing Gd substitution. The variations in interionic interactions clearly show the strength of magnetic interactions. UV Visible spectroscopy studies were also carried out to understand the optical properties of pristine and Gd substituted samples. The estimated direct band gap values were decreasing with an increase in Gd substitution and exhibited an inverse relationship with Urbach energy. The dielectric spectroscopy of $MnFe_{2-x}Gd_xO_4$ (x = 0.00, 0.02, 0.04) was studied at frequencies ranging from 500 Hz to 1MHz which will explain the electrical properties of this material. The study reveals that dielectric permittivity increases with Gd substitution and dielectric loss are inversely related to Gd substitution.

CONTENTS

List of Figures

List of Tables

Chapter 1
General Introduction

1.1 Dielectric Materials and Properties

A dielectric material is a substance that is a poor conductor of electricity, but an efficient supporter of an electrostatic field. Dielectric materials are used in the construction of radio frequency transmission lines. In practice, most dielectric materials are solids (mica, glass, plastic etc.). Some liquids and gases can serve as good dielectric materials. Dry air is an excellent dielectric and is used in variable capacitors and some types of transmission lines. When dielectrics are placed in an electric field, practically no current flows in them because unlike metals they have no loosely bound or free electrons that may drift through the material. Instead electric polarization occurs. The positive charges within the dielectric are displaced minutely in the direction of the electric field, and the negative charges are displaced minutely in the direction opposite to the electric field. This slight separation of charge, or polarization, reduces the electric field within the dielectric

1.1.1 Electric Dipole and Dipole Moment

A dipole is defined as two equal and opposite charges +q and –q separated by a distance r. A schematic representation of an electric dipole is shown in figure 1.1. The dipole moment is equal to the product of one of the charges and the separation between them [1].
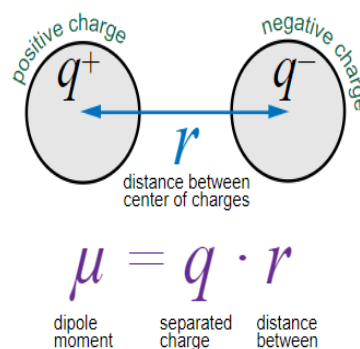
Figure 1.1 Schematic representation of dipole moment[2]

1.1.2 Dielectric constant

Dielectric constant refers to the measure of the degree to which a medium can resist the flow of charge. It is also known as the permittivity of the medium. The dielectric constant relies on the frequency of the alternating electric field or the rate of the change of the varying field. It is defined as the ratio of the electric displacement D to the electric field intensity E [1].

$$\varepsilon = \frac{D}{E} = \varepsilon_r \varepsilon_0 \qquad (1)$$

1.1.3 Dielectric polarization

Polarization is defined as the dipole moment per unit volume. Let N be the number of molecules per unit volume and μ be the dipole moment of the molecule [1]. Then polarization vector P is given as

$$P = N\mu \qquad (2)$$

1.1.4 Dielectric polaraizability

Dielectric polarizability is defined as the net dipole moment per unit applied electric field. Net dipole moment is proportional to the applied electric field [1].

1.1.5 Types of polarization

Polarization occurs due to several mechanisms. When a specimen is placed in an electric field, 4 types of polarizations occur in the dielectric material [1].

> 1. Electronic polarization
> 2. Ionic polarization
> 3. Dipolar or orientational polarization
> 4. Space charge polarization

➢ **Electronic polarization**

All orbiting electrons in the atom form a spherical cloud of negative charge that surrounds the positively charged nucleus. The negative charge of the electron cloud is homogeneously distributed on a sphere. When there is no influence of any external electric field, the centre of this sphere and the centre of the nucleus of the atom coincide.

When an external electric field of intensity E is applied to the atom, the atom is shifted towards the negative intensity of the field and the electron cloud is shifted towards the positive intensity of the field. This displacement of the nucleus and electron cloud in opposite directions on the application of electric field is electronic polarization [1].

> **Ionic polarization**

As the name ionic polarization occurs in ionic materials. It occurs when an electric field is applied to an ionic material then cations and anions get displaced in opposite directions giving rise to a net dipole moment called ionic polarization [1].

> **Dipolar or Orientational polarization**

When an external field is applied to the polar dielectric material, all the dipoles are aligned in the direction of the applied field. The polarization produced in polar dielectric material due to the application of an electric field is called orientational polarization. Orientational polarization depends on temperature [1].

> **Space charge polarization**

The space charge or interfacial polarization is produced by the separation of mobile positively and negatively charged particles under an applied field, which form positive and negative space charges in the bulk of the material or at the interfaces between different materials [3].

1.1.6 Frequency dependence of the polarizability

When a dielectric material is placed in the presence of an electric field, the dipoles attempt to maintain alignment with the field and this polarization process occurs as a function of the time given by

$$P(t) = P[1-\exp(-t/t_r)] \hspace{2cm} (3)$$

Where $P(t)$ represents the maximum polarization and t_r is the relaxation time for a particular relaxation process. The finite time required by each polarization mechanism is quite different. Electronic polarization is a rapid process and it occurs during every cycle of the applied voltage frequencies only electronic polarization is operative and it is also sometimes known as optical polarization [4].

Ionic polarization is due to the displacement of ions over a small distance in the presence of an applied field. Since the ions involved are heavier than the electron cloud, the time taken for displacement will be larger. The frequency with which ions are displaced is in the same order as lattice vibration frequency. If the frequency of applied voltage is less than 10^{13}Hz, both electronic and ionic polarization can be obtained.
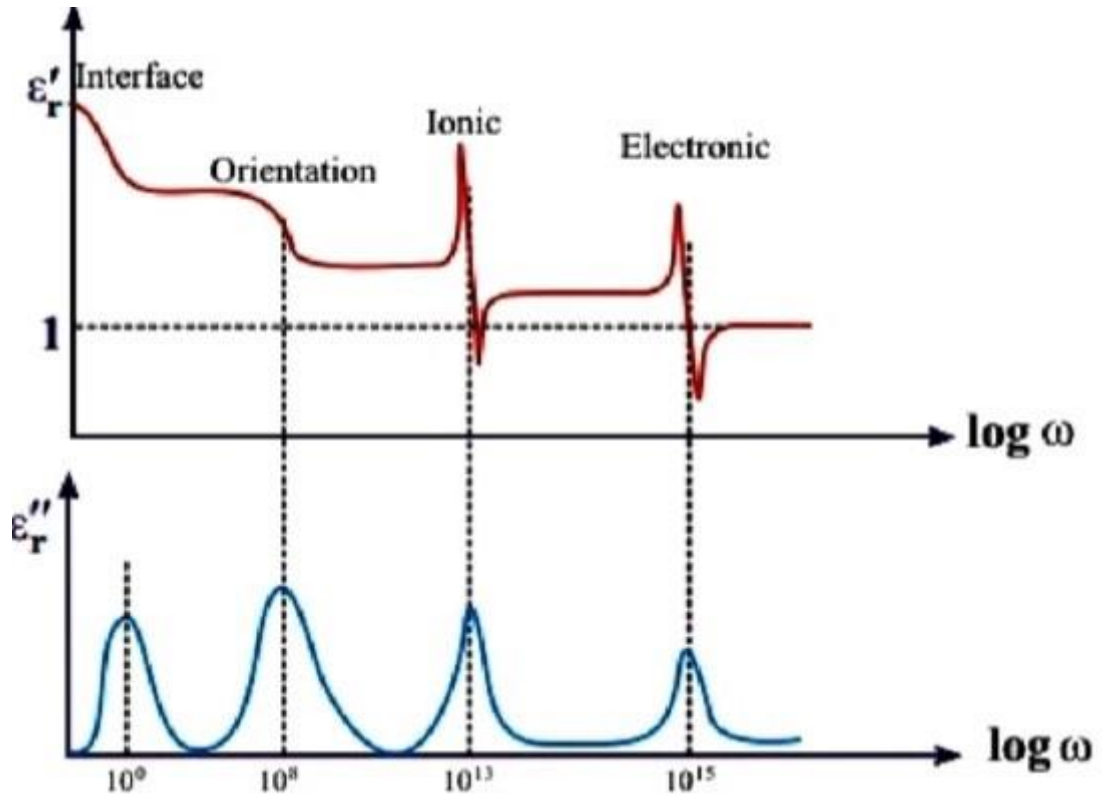
Figure 1.2 Frequency dependence of various polarization processes [5]

Orientation polarization is even slower than ionic polarization. Orientation polarization is likely to occur when the frequency of applied voltage is in the order of audio frequency range at a frequency of 10^4 Hz. Space charge polarization is the slowest process as it involves the diffusion of ions over several interatomic distances. The relaxation time for this process is related to the frequency of successful jumps of ions under the influence of an applied frequency of the order of 10^2 Hz.

It can be shown that in the optical frequency range the dielectric constant is obtained only as a result of electronic polarizability whereas dipolar and ionic contributions are small at high frequencies because of the inertia of the ions and molecules [4,6,7].

1.2 Ferrites

The history of ferrites (magnetic oxides) and their applications have been known for several centuries ago. The term ferrite is commonly used to describe a class of magnetic oxide compounds that contain iron oxide as a principal compound. Magnetite (Fe_2O_4), also called loadstone, is a genuine ferrite and was the first magnetic material known to the ancient people. Ferrites are hard, brittle, iron-containing and generally grey or black and are polycrystalline that is made up of a large number of small crystals. Ferrite nanoparticles belong to a broad group of magnetic materials and have wide applications in various fields, which ranges from biomedical to industrial. The most important properties of ferrites include high magnetic permeability and high electrical resistance. High magnetic permeability is used in antennas. High resistance to electricity is desirable in the cores of transformers to reduce the eddy current [8].

Depending on their properties, commercial ferrite is classified into two parts soft ferrites and hard ferrites. In which soft ferrites have low hysteresis losses, low coercivity, and high saturation magnetization. Hard ferrites have a large value of retentivity and coercivity. Ferrites are the combinations of one or more bivalent oxides with trivalent iron oxide. Most of them are stoichiometrically balanced. The ratio of bivalent and trivalent oxide is 1:1. Different types of ferrite have different chemical formulas. Ferrite exhibits strong ferrimagnetism because it possesses electrons of metal and oxygen ions on their lattice site with the opposite spin arrangement. As ferrites have different chemical compositions, their magnetic properties can be varied from one element to another as microscopic structures. Ferrites are non-conducting magnetic media because of their low eddy current and ohmic losses [8].

1.3 Classification of Ferrites

1.3.1 Based on Crystal Structure

Depending on the magnetic properties and crystal structure, ferrites are classified into two groups. According to the crystal structure, they are classified into four groups

1. Spinel
2. Hexagonal
3. Garnet

4. Ortho ferrite

❖ **Spinel Ferrites**:-Spinel ferrites are described by the chemical formula MFe_2O_4 where M stands for divalent metal ions. The crystal structure of spinal ferrite possesses two interstitial sites namely tetrahedral (A) and octahedral (B). This type of ferrites possesses a spinel structure with a cubic lattice. A variety of cations can be occupied at the tetrahedral A site and octahedral B site enabling wide variation in the properties of ferrites. M can be replaced by other divalent metal ions and we can have some spinel ferrites. Fe^{3+} ions can be replaced by other trivalent ions like Al^{3+}, Cr^{3+}, Ga^{3+} etc. Fe^{3+} ions can also be replaced by a combination of divalent and tetravalent ions. Inverse spinel has a closely related structure in which the A-site ions and half of the B-site ions switch places. Inverse spinel is thus formulated as $B(AB)O_4$, where the AB ions occupy octahedral sites, and the other B ions are on tetrahedral sites [9].
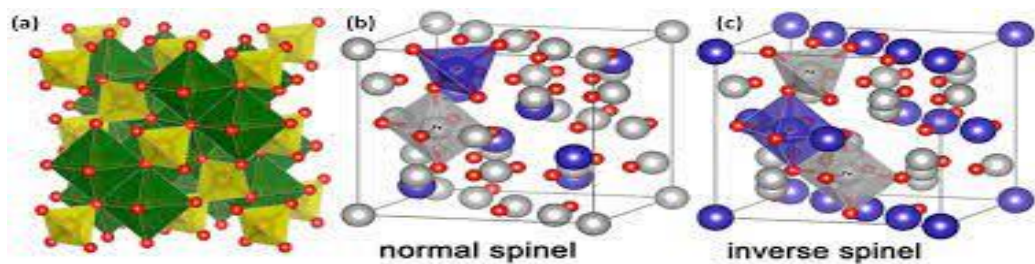
Figure 1.3 Structure of Spinel Ferrite [10]

❖ **Hexagonal Ferrites: -** Hexagonal ferrites are ferrimagnetic materials, and their magnetic properties are intrinsically linked to their crystalline structures. They have magnetocrystalline anisotropy that is the induced magnetization has a preferred orientation within the crystal size. Hexagonal ferrites are a class of magnetic oxides which have been widely used in recent years due to their application in microwave devices, magnetic recording media, etc. They are usually characterized by the formula $MFe_{12}O_{19}$ where M stands for elements like Ba, Sr, Pb or Ca, etc. This synthetic magnetic oxide in general shows a magneto plumbite structure with hexagonal symmetry. An interesting property of hexaferrite is its high coercivity which enables us to use them as permanent magnets [11].
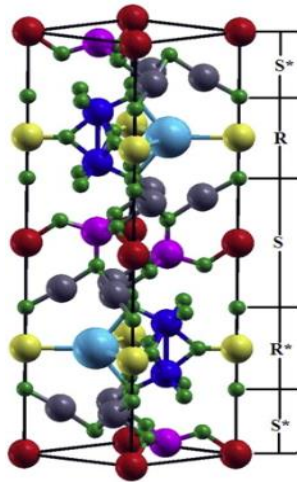
Figure 1.4 Structure of Hexagonal Ferrite [12]

❖ **Garnet Ferrites**:-The chemical formula for ferrimagnetic garnet is $Me_3Fe_5O_{12}$ where 'Me' is a trivalent ion such as rare earth or yttrium. The unit cell is cubic and contains eight molecules of $Me_3Fe_5O_{15}$. The metal ions are distributed over three types of sites. The Me ions occupy the dodecahedral sites (c sites), where they are surrounded by eight oxygen ions. The Fe^{3+} ions are distributed over the tetrahedral and octahedral sites in the ratio of 3:2. As in the case of spinel, the magnetic alignment results from super exchange interaction via the intervening oxygen ions. And the interaction is expected to be greater for short Me-O distance and closer the Me-O-Me angle is to 180°. On this, it is concluded that the interaction between the 'd' and 'a' cations are relatively strong. The total magnetic moments on a and b ions are aligned antiparallel and the moment on the c-ions are antiparallel to those on the d-ions [13].
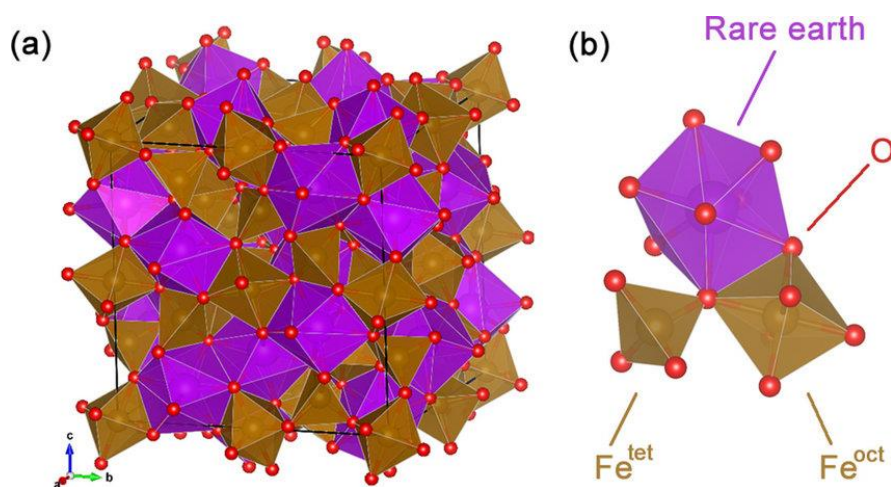
Figure 1.5 Structure of Garnet Ferrite [14]

❖ **Ortho Ferrites:-** Ortho-ferrites have the general formula $MeFeO_3$, Where 'Me' is a large trivalent metal ion such as a rare earth ion or yttrium. They crystallize in a distorted perovskite structure with an orthorhombic unit cell. These ortho ferrites show weak ferromagnetism, which has been attributed to the small canting in the alignment of two anti-ferromagnetic coupled lattices. The canting angle is of the order of 10^{-2} radian but is sufficient to introduce a small net ferromagnetic moment perpendicular to the anti-ferromagnetic axis.
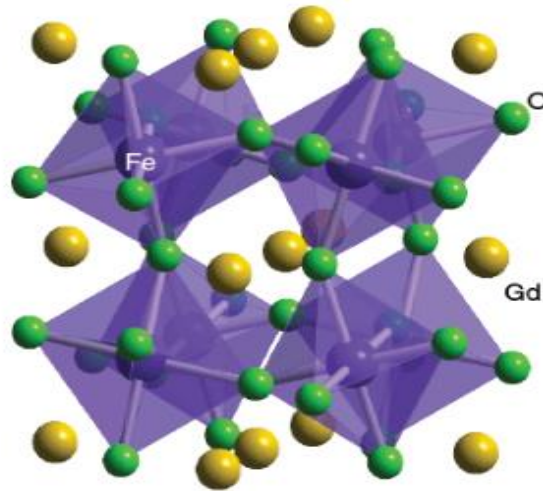
Figure 1.5 Structure of orthoferrite [15]

1.3.2 Based on Magnetic Properties

According to magnetic properties, they are two types

1. Soft ferrites
2. Hard ferrites

➤ **Soft ferrites:-**Soft ferrites have low coercitivity, so they easily change their magnetization and act as conductors of magnetic fields. All soft ferrites are ferrimagnetic materials with cubic crystal structures and they are represented by $MOFe_2O_3$. Where, M is a transition metal ion like iron, nickel, manganese, or zinc. Soft ferrites do not show permanent magnetism. Magnetic properties of soft ferrites arise from the interaction between metallic structures. These are extensively used in switch mode power supplies, inductors, convertors, etc. Mn-Zn ferrites ($MnZnFe_2O_4$) and Ni-Zn ferrites ($NiZn-Fe_2O_4$) are the most common examples of soft ferrites [4,16].

➢ **Hard ferrites:-**Ferrites that can sustain their magnetism after being magnetized are the hard ferrites which are also known as permanent magnets. These ferrites exhibit ferromagnetism even in the absence of an external field. Hard ferrites are composed of iron and barium or strontium oxides. They find applications in transformer cores, cathode ray tubes, small DC motors, compact torque devices, magnetic latches, etc. The most common hard ferrites are the M – type ferrites which exhibit a magneto plumbite structure and this crystal structure can be viewed as cubic blocks with the spinel structure and hexagonal blocks containing the metal ions. The most common examples of hard ferrites are barium ferrite ($BaO_6Fe_2O_3$) and strontium ferrite ($SrO_6Fe_2O_3$) [4,16]

1.4 Application of Ferrites

Ferrites are regarded as better magnetic materials than pure metals, because of their high resistivity, lower cost, easier manufacture and superior magnetization properties. Ferrites are extensively used in radar, audio-video and digital recording, memory cores of computers, satellite communication and microwave devices. Ferrite has vast applications from microwave to radio frequencies.

1. Ferrites are used in thermal sensing switches used in refrigerators, air conditioners, electronic ovens, etc.

2. The magnetostrictive property of ferrites is utilized in producing ultrasonic waves from a ferrite rod by the application of an alternating magnetic field.

3. The insulating property of ferrites finds their use in electric motors, they are also used as flat rings for loud speakers, wind screen wiper motors and correction magnets for TV.

4. Some ferrites possess a high rectangular hysteresis loop, so they are useful in the construction of computer memory systems for rapid storage and retrieval of digital information.

5. Mixed ferrites possess high resistivity and good magnetic coercivity [17].

1.5 Manganese ferrite

Researchers have been drawn to magnetic materials such as ferrites because of their unique electrical and magnetic properties. Among the different classes of ferrites, spinel ferrites are the ones who gained a permanent position in the research fields and technology because of their outstanding electrical and magnetic properties. Manganese ferrite is one of the important members of this ferrite family. It is a partial inverse spinal ferrite with about only 20% of the Mn^{2+} ions on the B (Octahedral) sites and the remaining 80% on the A (Tetrahedral) sites. The motivation behind the present study of manganese ferrite is due to their characteristic properties like high permeability, excellent chemical stability, low eddy-current loss, high coercivity etc. These properties enable us to apply them in high-frequency applications, magnetic storage devices, etc. High-density manganese ferrites are also important in technical applications such as coil or transformer core materials, and information and communication devices. And so on [17].

1.6 Literature review

Salar Ahmad *et.al.* successfully synthesized nanoparticles of $MnFe_2O_4$ from low-grade manganese ore through a solid state reaction route. The impact of sintering temperature on phase composition, particle size and also frequency on dielectric constant were investigated. The results show the presence of the spinel structure of manganese ferrite as a major phase for the sample sintered at 1200℃. The crystalline size increases with increasing sintering temperature. The surface morphology of the sample sintered at 1200℃ shows pyramidal and triangular shape grains. The Manganese ferrite phase becomes more relevant at high temperatures. Microstructure SEM images confirmed that the obtained manganese ferrite nanoparticles have porous and spongy type surfaces. Varying concentrations of iron and manganese have been found in the synthesized manganese ferrite along with some content of silica as an impurity. Some certain regions of the nanoparticles have certain thick layers of silica. The sample possesses a high dielectric constant and less dielectric loss at low frequency and low temperature. Finally, the synthesized material behaves like normal ferrite, that is, its conductivity is linearly increased with increasing frequency [18].

M Goodarz Naseri *et.al.* synthesized cubic structural manganese ferrite nanoparticles by a thermal treatment method followed by calcination at various temperatures from 723 K to 873 K. Polyvinyl pyrrolidone (PVP) was used as a capping agent to control the agglomeration of the nanoparticles. The characterization studies were conducted by X-ray diffraction and transmission electron microscopy etc. Fourier transform infrared spectroscopy confirmed the presence of metal oxide bands at all temperatures and the absence of organic bands at 873 K. Magnetic properties were demonstrated by a vibrating sample magnetometer (VSM), which displayed that the samples exhibited superparamagnetic and ferromagnetic behaviour [19].

Elangbam C. Devi *et.al.* Manganese ferrite nanoparticles have been synthesized by the low-temperature chemical co-precipitation method. The structural and optical properties of the nanoparticles were studied by using various techniques. XRD confirms pure spinel phase formation of the prepared sample. FTIR spectrum shows the characteristic bands of the spinel ferrite. Morphology of the nano ferrites was given by SEM image revealing that the particles are approximately spherical. The optical studies reveal that the nanoparticles show strong absorption around 450 nm wavelengths and the band gap calculated using the Tauc plot was found to be 1.4 eV, which is slightly smaller than those standard values. By changing certain parameters, the study on the optical properties of manganese ferrite nanoparticles gives a further possibility for application in various fields such as solar cells, optoelectronic devices, and photovoltaic and photocatalytic applications [20].

Mary Jacintha *et.al.* synthesized Nano-sized manganese ferrite ($MnFe_2O_4$) particles prepared by the sol-gel method by using natural polymers like wheat flour (WF) and potato flour (PF) as surfactants. Its structural, morphological, optical and magnetic characteristics were studied. A surface area test was also performed and the results obtained were discussed. Magnetic hysteresis loops confirmed the superparamagnetic behaviour for both samples. The average crystalline size was found to be 23 and 26 nm for $WF/MnFe_2O_4$ and $PF/MnFe_2O_4$ samples respectively. The catalytic activity of $MnFe_2O_4$ nanoparticles was carried out for the oxidation of benzaldehyde. Among these two samples, $PF/MnFe_2O_4$ shows a better response than $WF/MnFe_2O_4$ and both the samples were non-toxic to normal cells. The sol-gel method is better for the preparation of homogeneous pure and compositionally stoichiometric ferrites [21].

B. Aslibeiki *et.al.* manganese spinel ferrite nanoparticles were synthesized by solvothermal route based on the high-temperature decomposition of metal nitrates in the presence of different contents of Triethylene glycol. At the Nano scale, a magnetic multi-domain configuration is preferred. The magnetic moment of single-domain particles can be considered as a superspin, which is depending on the particle's volume. This simple and low-cost method can be applied to prepare large quantities of nanoparticles. Powder X-ray diffraction (PXRD) and transmission electron microscopy (TEM) confirm that nanoparticles with good crystalline quality were obtained. FTIR showed that polymer molecules have the tendency to form bonds with the surface of ferrite nanoparticles reducing the surface spin disorder, and then enhancing the saturation magnetization (M_S). Therefore, a much higher M_S value was observed compared with that of bare nanoparticles without surfactant. Increasing the initial content of the solvent decreases the agglomeration and enhances the nanoparticles' dispersion in the polymer [22].

Jianjun Li *et.al.* by using the sol-gel method synthesized $MnFe_2O_4$ spinel ferrite nanoparticles. The size-dependent magnetic properties and distribution of cations at the atomic level in such kinds of oxides were understood from his findings. $MnFe_2O_4$ nanoparticles were formed at a temperature of 400ºC with no exothermic peak in the TGA-DTA. It was proved by the differential thermal and Thermo galvanometric analysis. A phase transformation cannot be seen or obtained once the spinal ferrite occurs in the growth process. It was found that the powder X-ray diffraction patterns of the sample when calcined at 700ºC, they exhibit much closeness to the one obtained from standard spinel ferrite. But samples calcined at 450 to 500ºC show peaks that are much broadened. It was finalized that the occupancy ratio of Fe^{3+} ions at the octahedral site decreases with calcination temperature and was proved by Mossbauer studies [23].

Bhandare *et.al.* successfully synthesized $MnFe_2O_4$ with help of the citric acid-assisted sol-gel auto combustion method. It determines the structural and magnetic properties with respect to annealing temperature. The FESEM micrographs obtained an idea of the irregularity-shaped morphology and particle size distribution. When the sample was heated at 400ºC, the direct spinel structure with Mn^{2+} occupying the tetrahedral sites was evident from Rietveld's refinement of obtained XRD pattern, with the Mn^{2+} being partially oxidized to Mn^{3+}. As the annealing temperature increased, the extent of oxidation of Mn^{2+} to Mn^{3+} was found to increase. It results in the complete

decomposition of $MnFe_2O_4$ into α-Fe_2O_3 phase at an annealing temperature of 600ºC and above [24].

Abdullah *et.al.* synthesized $MnFe_2O_4$ by wet-milling under atmospheric conditions. Mechanical milling is an efficient, simple and energy-saving method for the mass production of nanoparticles. $MnFe_2O_4$ can be obtained from the milling of ferric chloride, hematite, iron nitrate, manganese oxide, manganese powders, etc. Fully stoichiometric $MnFe_2O_4$ nanocrystals were synthesized under an air atmosphere by using the wet milling technique. Here, the magnetization measurements showed that saturation magnetization of nanoparticles at 300K was lower than that of bulk $MnFe_2O_4$. This was due to the surface spin disorder. The blocking temperatures were found to be at room temperature. It indicated that $MnFe_2O_4$ nanocrystals prepared can be used for future room temperature magnetic device applications [25].

C Santhosh *et.al.* studied the solvothermal synthesis of $MnFe_2O_4$ – Graphene composite for investigation of its absorption and antimicrobial properties. Graphene manganese ferrite ($MnFe_2O_4$-G) composite was prepared by solvothermal process and was tested for the adsorption of Pb, and Cd ions by analytic methods. The adsorption of Pb and Cd ions reached equilibrium within 120 and 180 minutes at 37ºC with maximum adsorption of Pb and Cd at 5 and 7 respectively. This adsorption onto $MnFe_2O_4$–G was spontaneous, exothermic and feasible in the range of 27º to 47ºC. Also, the nanocomposite $MnFe_2O_4$ –G dispersion showed the highest antibacterial activity of 82 % compared to graphene showing 37 % cell loss. The results indicated that $MnFe_2O_4$-G is an excellent material for the removal of toxic heavy metal ions as well as used as an adsorbent and antimicrobial agent. The adsorption of Pb and Cd ions to the $MnFe_2O_4$-G surface followed the second-order kinetic model. The experimental data were well fitted and presented through the Langmuir isotherm model [26].

M A Shilpa *et.al.* studied the electrochemical characteristics of manganese ferrite ($MnFe_2O_4$) nanoparticles and were assessed using various electrochemical techniques. The electrode material comprising $MnFe_2O_4$ nanoparticles with a nanorod spinel structure was synthesized by the sonochemical route and the dimensions ranged from 16-24 nm. Various techniques were used to determine the characteristics of $MnFe_2O_4$ nanoparticles. HCl and NaOH were used as electrolytes to study the electrochemical behavior of nanoparticles. The specific capacitance values determine from the CV

curve. The result obtained demonstrate that HCl is a more appropriate medium for supercapacitor applications because of the consistent electrochemical redox reversibility and the $MnFe_2O_4$ electrode also obtained good results in sensor studies. The $MnFe_2O_4$ nanoparticles exhibited a higher photocatalytic activity during the degradation of methylene blue (96%) under irradiation with UV light compared with Drimaren yellow (7%). The result of the study suggests that $MnFe_2O_4$ nanoparticles are suitable for use in electrode materials in supercapacitor devices and as photocatalysis for degrading organic pollutants [27].

L. Zhen *et.al.* synthesized and performed the characterization of single-crystalline $MnFe_2O_4$nanorods using a surfactant-free hydrothermal route. It was well evident from the XRD studies that the synthesized material is pure, highly crystallized single-phase $MnFe_2O_4$.Analysis of the magnetic properties of these nanorods gave us saturation magnetization as 74 emu/g.It was inferred that growing 1-D nanostructures along an easy magnetization axis might be a simple way to boost magnetic properties though more research is required [28].

Patricia Rivas *et.al.* nanoparticles of $MnFe_2O_4$ were synthesized via the sol-gel method. The effects of the different calculations in the formation of the crystal structure and magnetic and optical properties were studied with different techniques. The XRD studies reveal the formation of a phase corresponding to cubic spinal structure in both samples and the presence of the second phase identified as Fe_2O_3, in the case of the sample with higher temperature treatment. The magnetization as a function of magnetic field studies shows saturation at low calcination temperature compared to the expected one. No significant differences were observed in the magnetic behaviour of the sample [29].

1.7 Motivation for the present work

An extensive investigation has been made on nanosized ferrites due to their broad range of applications in magnetism and electricity. Ferrites are used for multipurpose as it exhibits high magnetic permeability, high coercivity, high resistivity and corrosion resistance at room temperature. High magnetic permeability is extremely useful in the development of various components in antennas, televisions, and other applications. At room temperature, most ferrites exhibit hysteresis properties, which can be useful in the

development of efficient data storage systems in computers, laptops, and so on. High resistivity ferrites are desirable for use in the manufacture of transformers because they reduce eddy currents and thus allow transformers to be used in microwave regions. Aside from transformers, high insulating behaviour is advantageous in the manufacture of electric motors, loudspeakers, and other household necessities.

Ferrites can be classified into different groups based on their structural and magnetic properties. Based on their structural properties they can be classified into 4 classes - spinel, garnet, ortho, and hexagonal ferrites. Based on magnetic properties, ferrites are often classified as soft and hard, which refers to low or high coercivity of their magnetism respectively. Spinel ferrites have the general formula MFe_2O_4, where M represents a divalent metal such as Fe, Co, Ni, Mn, Cu, or Zn, or a combination of these ions. Spinel ferrites have an FCC unit cell, which has 96 interstices (64 tetrahedral and 32 octahedral) that are referred to as A and B sites. Research on Spinel ferrites is expanded due to their unique electrical, optical, dielectric, magnetic, and catalytic properties. Since they are ferrimagnetic and semiconductors, they can be considered magnetic semiconductors. They exhibit high Curie temperature, a large magnetocrystalline anisotropy, good thermal stability, and low chemical composition as well as high magnetic characterization, tunable size and shape, a high specific surface area, and so on. These properties are determined by the nature of the divalent cation in the spinel structure, the synthesis method, grain size, morphology and other factors. The unique properties of ferrites can be tuned through proper substitution with rare earth in Fe sites. The substitution with rare earth ions in the spinel structure makes it more significant than any other substitution system. A small amount of rare earth ions introduced are occupied in the octahedral sites of spinel ferrites. The most common synthesis methods of ferrites are the sol-gel method, combustion method, hydrothermal and co-precipitation method. The sol-gel method has several advantages over other methods such as high purity of chemical and morphological properties, homogeneity of products etc. This chemical and easiest method is known to be the versatile process for synthesizing oxide materials. By controlling the dependent parameters like pH value of the sol, temperature of the reaction, reagent concentration and time of reaction it is possible to vary the structural, electrical and optical properties of the product.

Manganese ferrite ($MnFe_2O_4$) is one of the well-known members of the ferrite family due to its strong magnetism and high resistivity. It is used in magnetic resonance

imaging, hyperthermia, magnetic recording and high-frequency electronic device applications. Magnetic and dielectric properties of manganese ferrite can be tuned through the substitution with proper elements in Mn/ Fe sites. In $MnFe_2O_4$, Fe^{3+} ions give a major contribution to both electricity and magnetism. Therefore, the substitution with suitable ions in Fe sites can be more effective to tune its electrical and magnetic properties favorably. The selection of these elements depends on their magnetic moment and ionic radii [30–32]. Rare earth elements are the most prominent substituent due to their high magnetic moment and large ionic radii. A small amount of rare earth ion substituted at the octahedral B site will enhance the electrical and magnetic properties. The coupling of unpaired electrons in the 4f subshell of rare earth elements with 3d subshell electrons of Fe changes their intrinsic electric and magnetic properties. Also, Rare earth ions with larger ionic radius when substituted may distort the structure which induces strain, as a result, electrical properties get modified. Among the rare earth elements, Gd ion is chosen as its ionic radii are high and magnetic near room temperature. Thus the substitution with Gd ions is expected to enhance both electrical and magnetic properties of $MnFe_2O_4$. The present work focuses on the study of influence of Gd substitution on the structural, optical and electrical properties of manganese ferrite.

Chapter 2

Synthesis Method and Characterization

2.1 Sol-gel synthesis

Ferrites are the group of materials with exceptional magnetic properties and are synthesized by different methods. These are sol-gel method, combustion method hydrothermal method, co-precipitation method and so on. In each method material shows various properties. Sometimes conditions of experiment are changed to obtain perfect ferrite materials. Here we used sol-gel method as synthesis method for the production of ferrite material. In sol-gel method, we used different fuels like glycine, citric acid and so on to obtain good and efficient ferrite products. The sol-gel process is a more chemical method for the synthesis of various nanoparticles and is one of the easiest methods.

This method is a versatile process used for synthesizing oxide materials. This synthesis method generally allows control of the texture, chemical, and morphological properties of the solids. This method also has several advantages over other methods. The major advantages of the sol-gel technique include molecular scale mixing, high purity of the precursors and homogeneity of the sol-gel products with a high purity of physical morphological and chemical properties. The sol-gel method is considered as a bottom-up approach that means atomic level particles combines and form metal salts. Sol-gel is the combination of two words sol and gel; during the synthesis process we can see both two forms [33].

 In a typical sol-gel process, a colloidal suspension, or a sol is formed from the hydrolysis and polymerization reactions of the precursors, which are usually inorganic metal salts or metal organic compounds such as metal alkoxides. Any factor that affects either or both of these reactions is likely to affect the properties of the gel. These factors, generally referred to as sol-gel parameters, includes type of precursor, type of solvent, water content, acid or base content, precursor concentration, and temperature. These parameters affect the structure of the initial gel and, in turn, the properties of the material at all subsequent processing steps. After gel formation, the wet gel can be optionally aged in its mother liquor, or in another solvent, and washed. The time

between the formation of a gel and its drying, known as aging, is also an important parameter. A gel is not static during aging but can continue to undergo hydrolysis and condensation. Furthermore, synthesis, which is the expulsion of solvent due to gel shrinkage, and coarsening, which is the dissolution and re precipitation of particles, can occur. These phenomena can affect both the chemical and structural properties of the gel after its initial formation [33].

The sol-gel method has become one of the most popular and important techniques to synthesize various types of new materials, including high ionic conductors with high homogeneity and purity. The versatility of the sol-gel method is due to the mixing of starting chemicals (precursors) in the solution form at much lower temperature which gives good control of various components at atomic level. This technique has been extensively used to prepare different types of new materials in the bulk, powders, sheets, fibers, thin films, etc., for various advanced technological applications. Thus, the sol-gel route is more suitable for the synthesis of glassy/amorphous and crystalline materials than conventional methods [33].

The sol-gel process consists of the following steps:

1. Hydrolysis and alcoholysis

2. Water and alcohol condensation and polymerization

3. Growth of particles

4. Agglomeration of particles followed by the formation of network throughout the liquid medium resulting in a thick gel

The first step in a sol-gel reaction is the formation of an inorganic polymer by hydrolysis and condensation reactions, i.e., the transformation of the molecular precursor into a highly cross-linked solid. Hydrolysis leads to a sol, a dispersion of colloidal particles in a liquid, and further condensation results in a gel, an interconnected, rigid and porous inorganic network enclosing a continuous liquid phase. This transformation is called the sol-gel transition. There are two possibilities to dry the gels. Upon removal of the pore liquid under hypercritical conditions, the network does not collapse and aerogels are produced. When the gel is dried under ambient conditions, shrinkage of the pores occurs, yielding a Xerogel. One of the highly

attractive features of the sol-gel process is the possibility to shape the material into any desired form such as monoliths, films, fibers, and monosized powders, and subsequently convert it into a ceramic material by heat treatment [33].

Aerogel:- One important parameter that affects a sol-gel product is the drying condition. Due to the surface tension of the liquid, a capillary pressure gradient is present in the pore walls and this may be able to collapse most of the pore volume when solvent is removed. One convenient way to avoid pore collapse is to remove the liquid from the pores above the critical temperature (Tc) and critical pressure (Pc) of the fluid, namely, supercritical drying. Under supercritical conditions, there is no longer a distinction between the liquid and vapor phases: the densities become equal; there is no liquid-vapor interface and no capillary pressure. This type of drying prevents the formation of a liquid-vapor meniscus which recedes during the emptying of the pores in the wet gels. The resulting dried gel, called an aerogel, has a pore volume similar to that of the wet gel [33].

Xerogel:- Conventional evaporative drying induces capillary pressure associated with the liquid-vapor interface within a pore, causing shrinkage of the gel network. In a sample with a distribution of pore sizes, the resultant differential capillary pressure often collapses the porous network during drying. The dried sample often has low surface area and pore volume [33].

Cryogel:- Another way of avoiding the presence of liquid-vapor interface is to freeze the pore liquid and sublime the resulting solid under vacuum. In this method, the gel liquid is first frozen and thereafter dried by sublimation. Therefore, the formation of a liquid-vapor meniscus is prevented. The materials obtained are then also termed cryogels. Their surface area and mesopore volume tend to be smaller than those of aerogels, although they remain significant. However, freeze-drying does not permit the preparation of monolithic gels. The reason is that the growing crystals reject the gel network, pushing it out of the way until it is stretched to the breaking point. It is this phenomenon that allows gels to be used as hosts for crystal growth. The gel is so effectively excluded that crystals nucleated in the pore liquid are not contaminated with the gel phase; the crystals can grow up to a size of a few millimeters before the strain is so great that macroscopic fractures appear in the gel. However, the gel network may eventually be destroyed by the nucleation and growth of solvent crystals, which tend to

produce very large pores. To attenuate this event, a rapid freeze process known as flash freezing has been developed. It is also important that the solvent has a low expansion coefficient and a high pressure of sublimation [33].
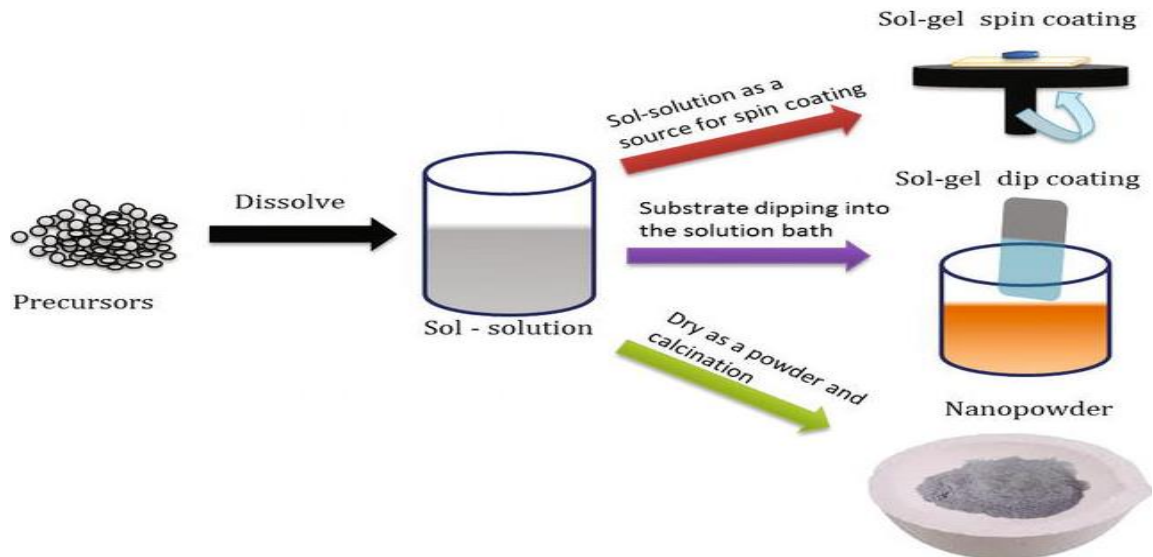
Figure 2.1 Schematic representation of sol-gel method [34]

Advantages of Sol-Gel Process

1) Low-temperature processing and consolidation is possible.

2) The homogeneity of the final product at the atomic level

3) Sintering at low temperature is also possible.

4) Better homogeneity and phase purity compared to the traditional ceramic method.

5) High-purity materials are obtained by using highly pure reagents.

6) Ability to control the composition on molecular scale.

7) Possible to synthesis complex composition materials and provide a coating over complex geometries.

Disadvantages of Sol-Gel Process

1) Raw materials for this process are expensive (in the case of metal alkoxides) compared to mineral based metal ion sources.

2) Products would contain high carbon content when organic reagents are used.

3) Since several steps are involved, close monitoring of the process is needed.

2.2 X-ray Diffraction Technique (XRD)

Wilhelm Roentgen who called them x-rays because their nature at first was unknown. So x-rays are also called Roentgen rays. X-ray diffraction in crystal was discovered by Max Von Laue. The wavelength range is 10^{-7} to about 10^{-15} m. The penetrating power of x-rays depends on energy also, there are two types of x-rays 1: Hard x-rays; which have high frequency and have more energy. 2: Soft x-rays; which have less penetrating and have low energy. X-ray diffraction technique is one of the easiest tools for measuring nanostructure. Materials are different by their unique structure, this structure can be studied using XRD [35].

Diffraction is the breaking up of a ray of light into alternately dark and light bands or the colours of the spectrum, as when it is deflected at the edge of an opaque object. The bands are called diffraction bands. XRD analysis is the analysis of the internal structure of crystals by utilizing the diffraction of X-rays caused by the regular atomic lattice of the crystal. These analytical techniques reveal information about the crystallographic structure, size, chemical composition, and physical properties. These techniques are based on observing the scattered intensity of an x-ray beam hitting a sample as a function of incident and scattered angle, polarization, and wavelength or energy [35].

Solids are characterized by their definite shape, mechanical strength, and rigidity. Hence solids are classified into two types these are crystalline and amorphous solids. A crystalline solid is one in which the constituent structural units are arranged in a definite geometrical configuration characteristic of the substance. Amorphous solids have no definite geometrical form and are regarded as supercooled liquids with high viscosity. A crystal lattice is made up of regular planes of atoms equal distance apart. Since the wavelengths of x-rays are comparable to the interatomic distances, Laue suggested that it might be possible to diffract x-rays by crystals. This suggestion came out to be true when Bragg succeeded in diffracting x-rays from sodium chloride crystal [35].

Bragg`s Equation

In 1983 W.L. Bragg and W.H Bragg worked out a relation to determine interatomic distances from x-ray diffraction patterns. This relation is known as Bragg`s equation.

1: The x-ray diffraction from atoms in crystal planes obeys the laws of reflection.

2: The two rays reflected by successive planes will be in phase if the extra distance travelled by the second ray is an integral number of wavelength
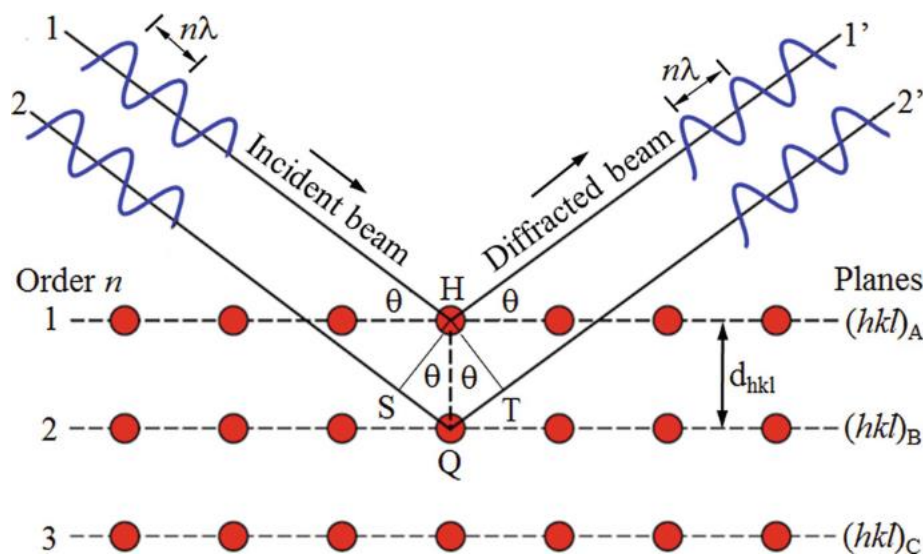
Figure 2.2 Schematic diagram of Bragg's law [36]

According to Bragg`s law,

$$\lambda = 2d\sin\theta \qquad (4)$$

    d- Stands for interplanar distance between crystalline planes in crystal lattice

    λ- Wavelength of the x-ray

    θ- Angle

The obtained diffracted pattern gives an idea about the crystallographic symmetry of the material structure [35].

X-ray diffraction have mainly categorized into three methods

    1: Laue method

    2: Rotating crystal method

3: powder method

> **Laue method**

The Laue method is the simplest and oldest of the x-ray diffraction method. In this method analysis of crystal structure is done by using a single, fixed crystal irradiated by a continuous spectrum of x-ray.
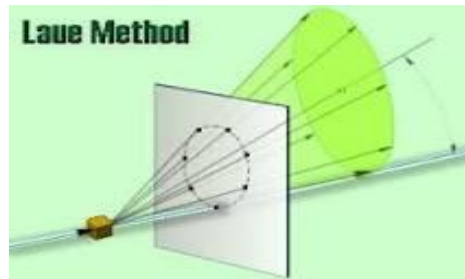
Figure 2.3 Laue method

> **Rotating crystal method**
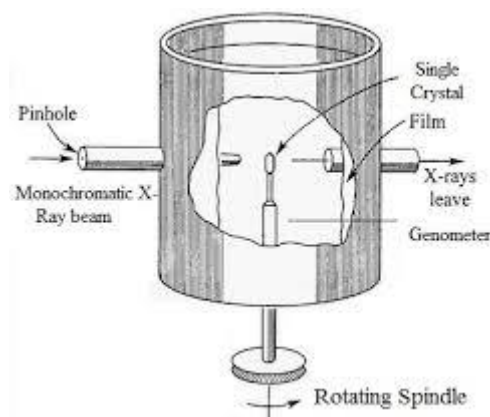
Figure 2.4 Rotating Crystal Method [37]

In the case of rotating crystal method, wavelength of x-ray is fixed but the angle of diffraction is kept varied. The crystal is rotating gradually by its own axis and changes their angle of diffraction. This method is only applicable if a single undistorted crystal.

> **Powder method (Debey- Scherrer Method)**

To avoid the limitations of these two methods powder method is derived. The powder consists of many small crystals which are oriented in a possible direction. In this method, no rotation is necessary because the powder contains microcrystal

arrangements in all orientation. Nowadays powder diffraction method is commonly used due to its simplicity.
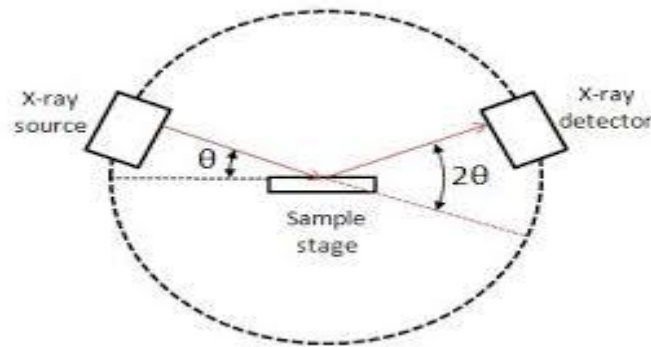
Figure 2.5 Debye Scherrer Method [38]

W-H plot helps to measure the crystallite size and micro-strain product in the crystal structure. It supports the structural analysis and calculation made using the Debye-Scherrer equation.

The crystalline size in the absence of inhomogeneous strain,

$$D = \frac{k\lambda}{\beta cos\theta} \qquad (5)$$

D is the crystalline size of the particle; k is defined as shaping factor crystals. The shaping factor varies from 0.89 to 0.9 based on their crystal lattice. Λ represents the wavelength of x-ray source. β corresponds to full width half maximum of diffraction of peak and β must be in radian. θ represents the position of the diffraction peak [35].

2.2.1 X-ray Diffractometer

An X-ray diffractometer, or XRD machine, is a device for analyzing and measuring the structure of materials. X-rays have high energy and short wavelength when compared to visible light making them ideal for probing the interplanar distances in crystalline materials. Application of Bragg's law in different ways can lead us to structural analysis and x-ray spectroscopy in which the latter deals with the determination of the wavelength λ of the radiation used with known values of spacing d, and measuring θ for a given crystal. X-ray diffraction represents a non-destructive technique for examining large varieties of materials such as catalysts, thin-film coatings, polymers, pharmaceuticals, and so on. XRD represents an opening path to certain applications

such as determining crystal structures using Rietveld refinement, characterise thin film samples, and Tailored X-ray diffractometers that can measure various sample sizes and geometries.
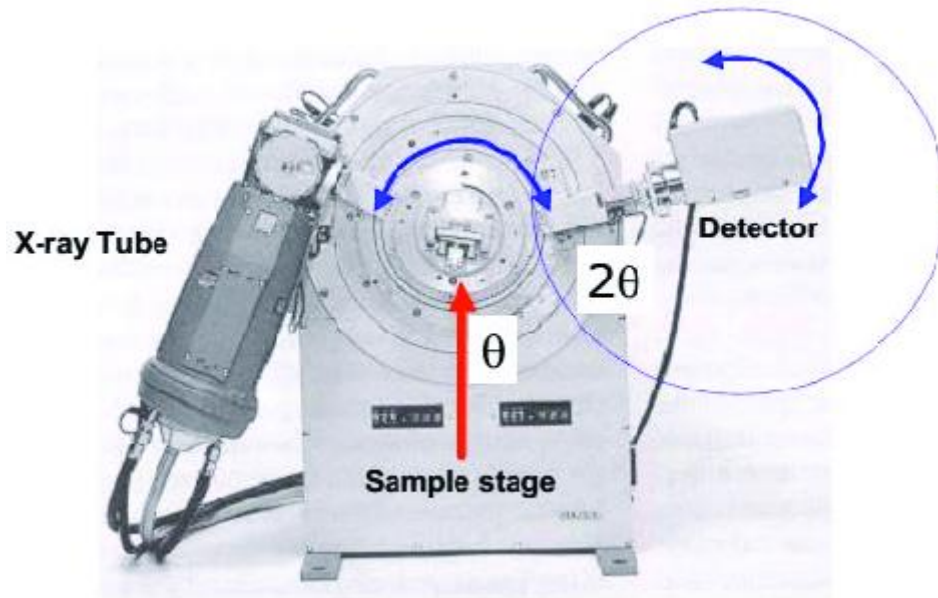
Figure 2.6 Schematic diagram X-ray Diffractometer [39]

An X-ray diffractometer consists of an X-ray diffraction goniometer, several amplifiers, and a detector in addition to the X-ray generator and the X-ray tube. An X-ray diffractometer's geometry is such that the sample rotates at a particular angle in the direction of the collimated X-ray beam, while the X-ray detector is placed on an arm to collect data [35].

Advantages of PXRD

1) Rapid and powerful method for the identification of unknown minerals and materials.

2) XRD measurement instruments are widely available.

3) Interpreting the resulting data is relatively straightforward.

4) Minimal sample is required for analysis.

Disadvantages of PXRD

1) The sample should be homogeneous.

2) It requires access to standard reference data.

3) Preparation of samples often requires grinding them down to a powder [35]

2.2.2 Rietveld Refinement

During X-ray diffraction analysis the pattern can be varied due to the instrument parameter. To obtain actual results we have to refine these varying parameters. Rietveld Refinement is a technique described by Hugo Rietveld for the characterization of crystalline materials. The crystal structure is refined by fitting the entire profile of the diffraction pattern to a calculated profile using a least-square approach. It is possible to determine the accuracy of a crystal structure model by fitting a profile to a 1D plot of observed intensity versus angle. It is important to remember that Rietveld refinement requires a crystal structure model. It can be used to find structural details such as unit cell, dimension, phase quantities, crystalline size or shapes, atomic coordinates or bond length, etc.

Before exploring Rietveld refinement, it is necessary to establish a greater understanding of powder diffraction data and what information is encoded with it. A typical diffraction pattern can be described by the position, shape, and intensities of multiple Bragg's reflections. Each of the three mentioned properties encodes some information relating to the crystal structure, the properties of the sample and the properties of the instrumentation. The structure of a powder pattern is essentially defined by instrumental parameters and two crystallographic parameters unit cell dimensions and atomic content and coordination.

1. Establish peak positions: Bragg peak positions are established from Bragg's law using the wavelength and d-spacing for a given unit cell.

2. Determine peak intensity: Intensity depends on the structure factor, and can be calculated from the structural model for individual peaks. This requires knowledge of the specific atomic coordination in the unit cell and geometrical parameters.

3. Peak shape for individual Braggs peaks: Represented by functions of the FWHM called the peak shape functions.

4. Peak width: Peak width or full width half maximum (FWHM) of diffraction peak is another important parameter in diffraction patterns. We have the formula to describe FWHM with angular dependence given below,

$$(FWHM)_k = U\tan^2\theta_k + V\tan\theta_k + W \qquad (6)$$

U, V, and W are adjustable parameters. Refining these parameters will help to fit the peak width in a good manner [40,41].

2.3 UV-Visible Spectroscopy

UV spectroscopy refers to absorption spectroscopy or reflectance spectroscopy in UV visible range (200nm-800nm). The principle of UV-visible spectroscopy is based on the absorption of ultraviolet light or visible light by chemical compounds. This results in the production of distinct spectra. Spectroscopy is based on the interaction between light and matter. This method is complementary to fluorescence spectroscopy, which deals with the transition from the excited state to the ground state. Absorption measures transition from the ground state to the excited state. The Beer-Lambert law is the principle behind absorbance spectroscopy.

Beer's law

This law states that the absorbance is proportional to the path length through the sample and the concentration of the absorbing species.

$$A = \varepsilon bc \qquad (7)$$

A- Absorbance, ε- Molar absorptivity, b- Length of the light path and c- Concentration

Lambert's law

This law can be stated as when a beam of light is allowed to pass through a transparent medium. The ratio of decrease of intensity with the thickness of the medium is directly proportional to the intensity of light. Mathematically Lambert's law can be expressed as

$$-\frac{dI}{dx} \propto I \qquad (8)$$

Or

27

$$-\frac{dy}{dx} = \text{KI} \qquad\qquad (9)$$

Tauc plot

The tauc plot is used to determine the optical bandgap or tauc gap in semiconductors. The tauc plot is often used to characterize the practical optical properties of amorphous materials. Jan Tauc showed that the optical absorption spectrum of amorphous germanium resembles the spectrum of the indirect transitions in crystalline germanium and proposed an extrapolation to find the optical bandgap of these crystalline-like states. Typically a tauc plot shows the quantity $(\alpha h\nu)^r$ where α is the absorption coefficient of the material it is given by$(\alpha)^{1/r}$. The value of the exponent $1/r$ denotes the nature of the transition.

r =1/2 for direct allowed transition

r =3/2 for direct forbidden transition

r =2 for indirect allowed transition

r =3 for indirect forbidden transition

The resulting plot has a distinct linear region that, extrapolation to the abscissa, yields the energy of the optical bandgap of the material.
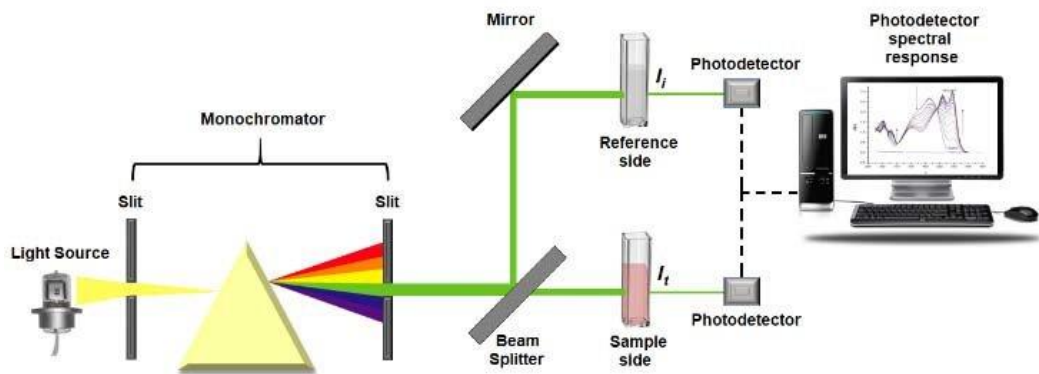
Figure 2.7 Schematic diagram of UV Visible spectroscopy [42]

UV-visible spectroscopy is a widely used technique in many areas of science for example bacterial culturing, drug identification and nucleic acid purity checks and quantitation etc. Here we can study the optical properties of m materials like reflection, absorption and transmission. This method under the framework of mie theory is used

to determine particle size and size distribution. The UV-visible absorption is used to characterize the kinetics of formation and final colloid stability.

UV-visible spectroscopy is a widely used technique in many areas of science for example bacterial culturing, drug identification and nucleic acid purity checks and quantitation etc. Here we can study the optical properties of materials like reflection, absorption and transmission. This method under the framework of mie theory is used to determine particle size and size distribution. The UV-visible absorption is used to characterize the kinetics of formation and final colloid stability [43].

2.4 Dielectric Spectroscopy

Dielectric spectroscopy is also known as electrochemical impedance spectroscopy. It is frequently used to study the response of a sample subjected to an applied electric field of fixed or changing frequency. D S describes the dielectric properties of a material as a function of frequency. Different types of DS are available commercially. All instruments are working in the same principle. It is based on the interaction of an external field with the electric dipole moment of the sample, often expressed by the permittivity. It is also an experimental method of characterizing electrochemical systems. This technique measures the impedance of a system over a range of frequencies, and therefore the frequency response of the system, including the energy storage and dissipation properties, is revealed. Often, data obtained by electrochemical impedance spectroscopy (EIS) is expressed graphically in a Bode plot.
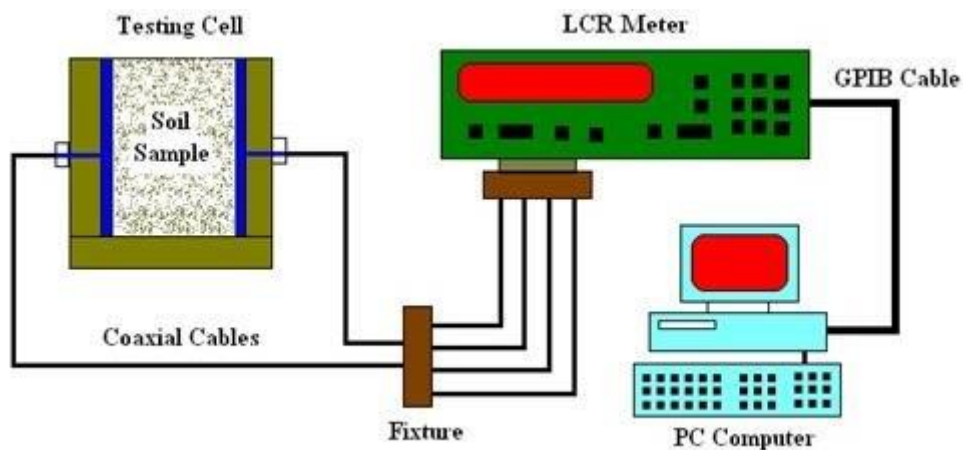
Figure 2.8 Schematic diagram of Dielectric measurement [44]

Impedance is the opposition to the flow of alternating current (AC) in a complex system. A passive complex electrical system comprises both energy dissipater (resistor) and energy storage (capacitor) elements. If the system is purely resistive, then the opposition to AC or direct current (DC) is simply resistance. Materials or systems exhibit multiple phases.

Mainly three methods are used to apply electric field to the sample. Applying a step function of voltage in each time interval are noted. This time-dependent result is converted into frequency-dependent data by Fourier or Laplace transforms. To get good dielectric measurements sample should be placed between two electrodes with good contact. Impedance spectroscopy helps to study the dielectric properties of solids in different conditions like frequency of applied electric field, oxygen partial pressure, temperature of the sample and microstructures of material and so on [45].

Chapter 3
Result and Discussion

3.1 Synthesis of Gd Substituted Manganese Ferrite

Gadolinium substituted Manganese ferrite ($MnFe_{2-x}Gd_xO_4$, x = 0.00, 0.02 and 0.04) was synthesized by citrate assisted sol-gel method. Manganese nitrate ($Mn(NO_3)_2$), Iron Nitrate ($Fe(NO_3)_3$) and Gadolinium Oxide (Gd_2O_3) are taken as the metal precursors and stoichiometric amounts of these precursors were dissolved in demineralized water separately. Along with these, citric acid and ethylene glycol are added and they act as fuels which help to gel formation. The entire precursor solution is then placed in a magnetic stirrer at 80^0C for 30 minutes to get a homogeneous solution. Then the solution is placed on a hot plate and heated the solution around 240^0C until the dry powder is formed. Later, the resultant powder is transferred into an agate mortar and thoroughly ground to get fine powders. A small amount of powder is ground with polyvinyl alcohol and pelletized into circular shape discs by Hydraulic press. The remaining powder and circular discs were sintered at 500^0C for 5 hours for densification. After densification, the powder is again ground by agate mortar.

For structural studies, XRD measurements were carried out by Bruker X-Ray Diffractometer. UV-Visible absorption studies were carried out by JASCO 750 UV Visible spectrophotometer in the wavelength range of 200 to 800 nm. Room temperature dielectric studies were carried out by HIOKI IM 3570 impedance analyzer.

3.2 XRD Analysis

The phase of the obtained powder is identified using the Qualx 2.24 software, which is freely available to all students at http://www.ba.ic.cnr.it/softwareic. Figure 3.1 shows the results obtained from the qualx software. From the phase identification studies, it is confirmed that $MnFe_2O_4$ prepared by the sol-gel method is well matched with COD ID: 2300618. From the crystallographic open database, it is seen that pristine $MnFe_2O_4$ exhibits a cubic spinel structure with space group Fd-3m.
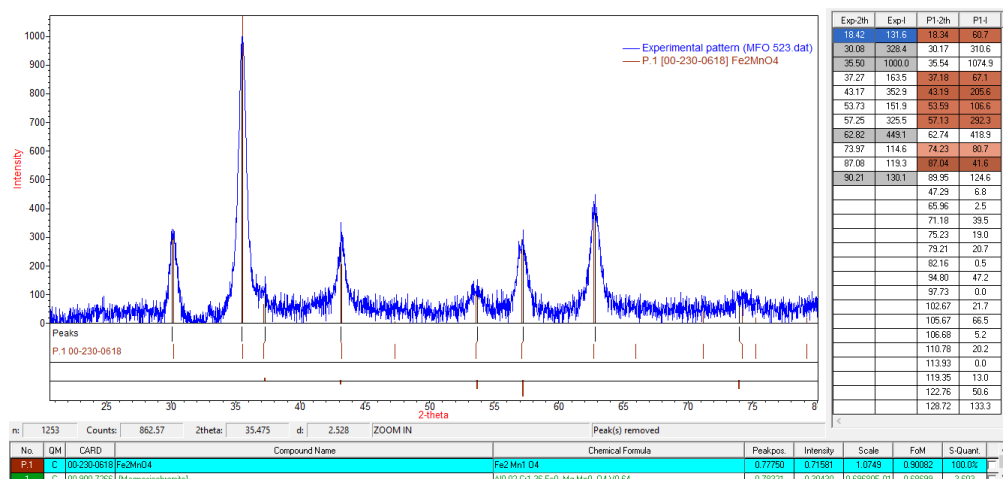
Figure 3.1 Phase identification of MnFe₂O₄ by Qualx Software
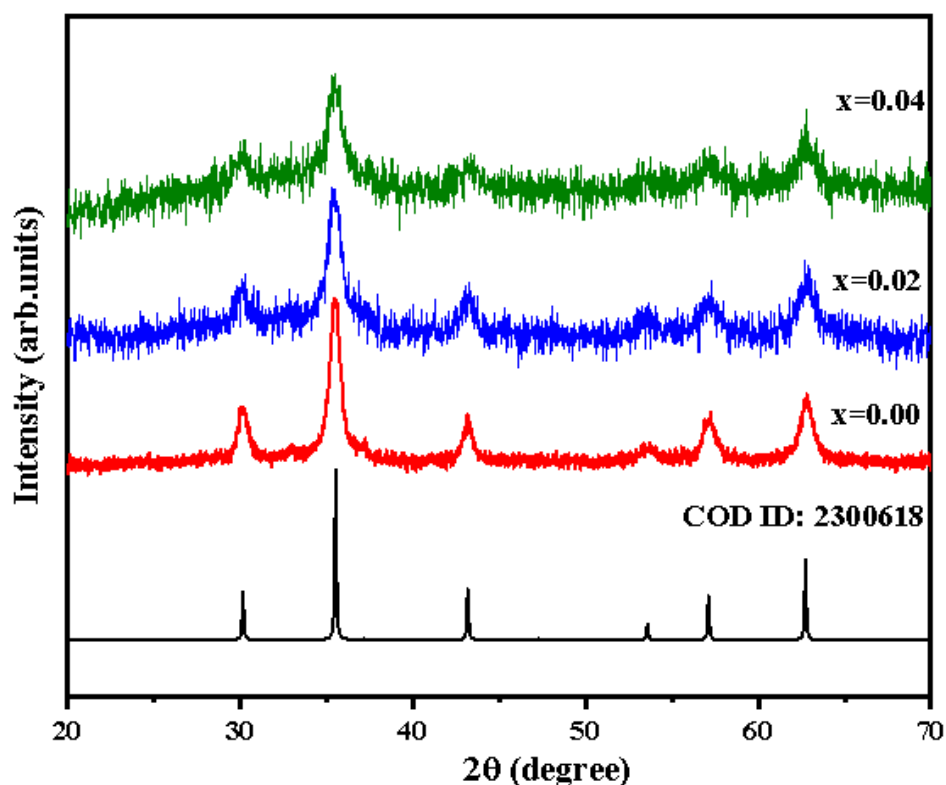
Figure 3.2 XRD pattern of MnFe$_{2-x}$Gd$_x$O$_4$ (x = 0.00, 0.02, 0.04)

The x-ray powder diffraction patterns of pristine and Gd^{3+} substituted $MnFe_2O_4$ are shown in figure 3.2. The XRD pattern shows that both pristine and Gd^{3+} substituted $MnFe_2O_4$ have a cubic spinel structure with a Fd-3m space group. All of the XRD patterns agree with the crystallographic open database COD ID: 2300618. It is observed

that the characteristic peaks of $MnFe_2O_4$ become broader and shifted towards lower angle region with Gd substitution. This broadening indicates that the crystallite size of $MnFe_2O_4$ decreases with Gd substitution. The shift of characteristic peaks attributes to the increase of lattice parameter with Gd substitution.
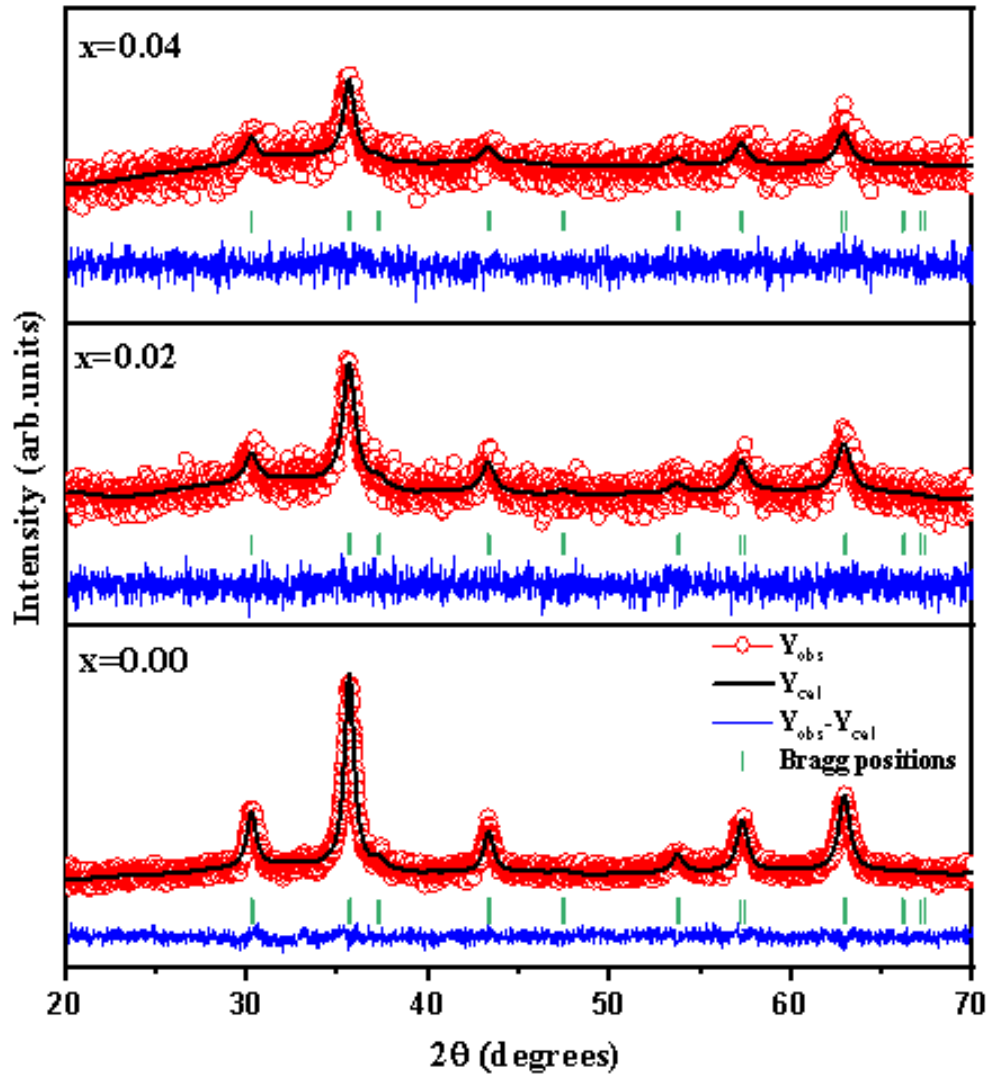
Figure 3.3 Rietveld refined x-ray powder diffraction patterns of $MnFe_{2-x}Gd_xO_4$
(x = 0.00, 0.02, 0.04)

In order to explain the crystalline size and lattice constant variation, XRD patterns of Gd substituted $MnFe_2O_4$ samples were refined by the Rietveld method. Figure 3.3 shows the Rietveld refined XRD pattern of Gd substituted $MnFe_2O_4$ samples using the Full prof software. It is seen that the experimental pattern of all the samples was exactly fitted with the theoretical calculated XRD pattern.

33

The average crystallite size is calculated using Debye - Scherrer's equation.

$$D = \frac{K\lambda}{\beta cos\theta} \qquad (10)$$

Where D is the average crystallite size in nanometers, k is the shape factor (0.9 for a cubic lattice), λ is the wavelength of incident radiation, β is the full-width half maximum of the peaks in radians, and θ is the corresponding angle of Bragg reflection peaks. Crystallite size calculated from Debye –Scherrer's equation is shown in table 3.1 of $MnFe_{2-x}Gd_xO_4$ (x = 0.02, 0.04) samples. From the table, it is evident that the average crystallite size decreases with Gd^{3+} substitution in the Fe sites of $MnFe_2O_4$. The formation of an additional Gd-O bond in the crystal lattice is the main reason for decreased crystallite size of $MnFe_2O_4$ with Gd^{3+} substitution. Since the bond energy of Gd^{3+} - O^{2-} is greater than that of Fe^{3+} - $O^{2-,}$ more energy is required for the Gd^{3+} substitution in place of Fe^{3+} ions to form a Gd^{3+} - O^{2-} bond and complete the crystallisation, which reduces the crystallite size of the material.

With Gd substitution in Fe sites, a shift in the characteristic peak corresponding to the (311) plane is also observed. This shift explains how the $MnFe_2O_4$ lattice parameter changes with Gd substitution. The lattice parameter and cell volume of $MnFe_{2-x}Gd_xO_4$ obtained from Rietveld's refinement of XRD patterns are included in Table 3.1. It is observed that the lattice parameter and cell volume of the $MnFe_2O_4$ increase with Gd^{3+} substitution. This increment can be attributed to the replacement of Fe^{3+} ions with Gd^{3+}(0.938), which has larger ionic radii than Fe^{3+} (0.645). The incorporation of larger ionic radii can cause structural distortion, which induces strain in the lattice, resulting in an increased lattice parameter. This indicates that the incorporation of larger ions in lattice sites expands the lattice. Thus, the main effect of Gd substitution in $MnFe_2O_4$ is lattice expansion and decreased crystallite size. Both of these effects point to the presence of strain-induced in the lattice.

Table 3.1 Crystallite size and lattice constant of $MnFe_{2-x}Gd_xO4$

(x = 0.00, 0.02, 0.04)

Concentration	Crystallite size (nm)	Lattice constant (Å)	Cell Volume (Å^3)
0.00	14.04	8.3562	583.48
0.02	10.16	8.3598	584.24
0.04	11.02	8.3601	584.29

The Scherrer formula considers only the effect of crystallite size on XRD peak broadening, but it says nothing about the lattice microstructure properties, i.e. the intrinsic strain that develops in nanocrystals due to point defects, grain boundaries, triple junctions, and stacking faults. Thus, the Williamson Hall method (W-H method) is employed to analyse and evaluate induced lattice strain in $MnFe_2O_4$ with Gd substitution. In this method, line broadening is expressed as,

$$\beta_{hkl} \cos \theta_{hkl} = \frac{k\lambda}{D} + 4\varepsilon \sin \theta_{hkl} \qquad (11)$$

Where ε is the strain effect on the lattice. The line broadening is based on two factors: crystallite size and crystal lattice strain. The above equation is a straight line equation. The slope of the W-H plot indicates the type and magnitude of intrinsic strain, whereas the intercept indicates crystallite size. The graph between $4 \sin \theta_{hkl}$ with $\beta_{hkl} \cos \theta_{hkl}$ for Gd substituted $MnFe_2O_4$ are shown in figure 3.4.
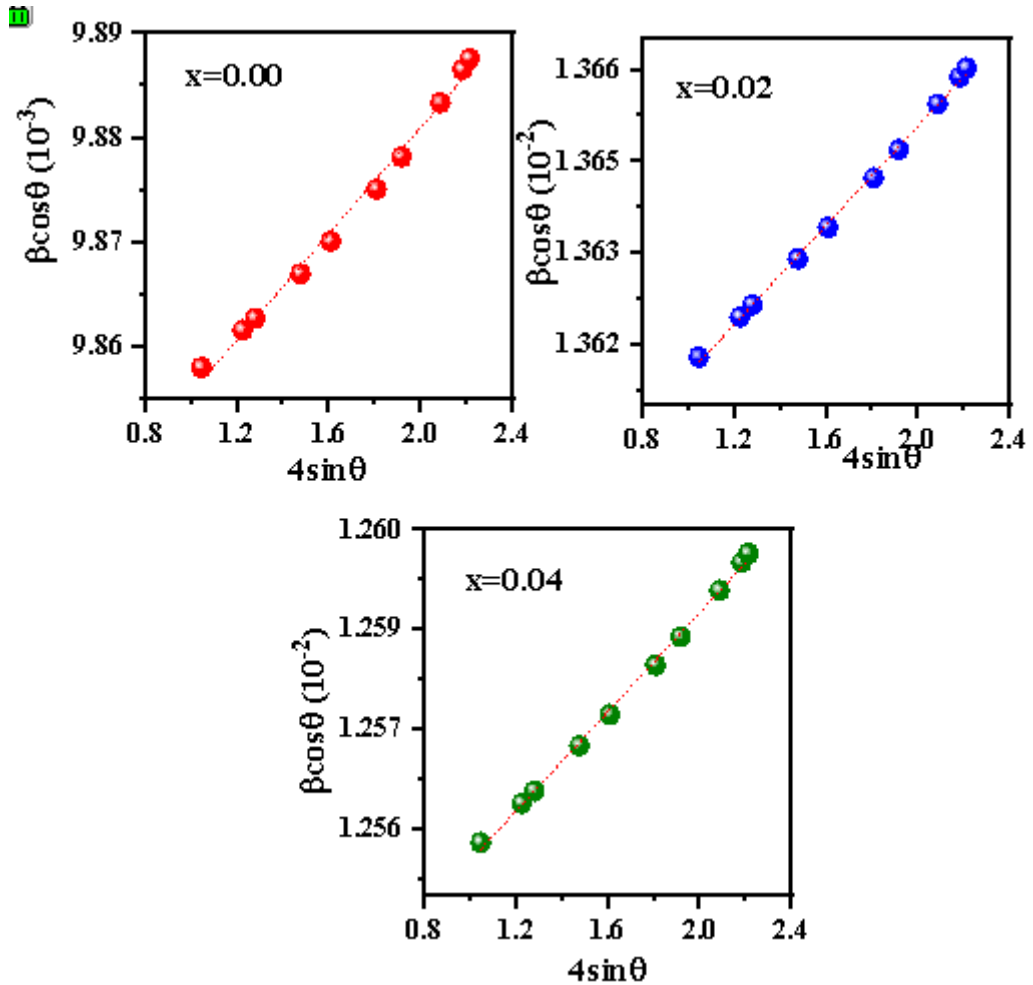

Figure 3.4. W-H plot of MnFe2-xGdxO4 (x = 0.00, 0.02, 0.04)

The crystallite size and lattice strain of $MnFe_{2-x}Gd_xO_4$ obtained from W–H plots are shown in table 3.2. It can be seen that the positive slope exists for Gd substituted $MnFe_2O_4$, indicating the presence of tensile strain. It is also observed that the crystallite size first decreases and then increases with Gd substitution, however, the increase is less than that of pristine $MnFe_2O_4$. This variation in crystallite size is attributed to induced strain in the lattice, which also exhibits a variation similar to the variation in crystallite size with Gd substitution.

Table 3.2 Crystalline size and strain of $MnFe_{2-x}Gd_xO_4$ (x = 0.00, 0.02, 0.04)

Concentration	Crystallite size (nm)	Strain (10^{-5})
0.00	14.10	2.53
0.02	10.21	4.06
0.04	11.08	3.72

Table 3.3 Occupancies obtained from Rietveld Refinement of $MnFe_{2-x}Gd_xO_4$ (x = 0.00, 0.02, 0.04)

x	Occupancies						Missing ions %		χ^2
	MnT	MnO	FeT	FeO	GdO	O	Mn	Fe	
0.00	0.0139	0.0276	0.0287	0.0539	-	0.1667	0.5	1.2	1.37
0.02	0.0139	0.0273	0.0243	0.0552	0.0008	0.1667	1.9	5.7	1.04
0.04	0.0139	0.0275	0.0302	0.0490	0.0017	0.1667	1.16	4.5	1.06

Metal ions occupy two sites in spinel ferrites, namely tetrahedral sites and octahedral sites. In order to determine the distribution of cations and anions, occupancies of $MnFe_{2-x}Gd_xO_4$ (x = 0.00, 0.02, 0.04) are evaluated from Rietveld analysis and shown in table 3.3. It can be seen that Mn^{2+} ions and Fe^{3+} ions can be found in both tetrahedral and octahedral sites. Since octahedral sites are larger than tetrahedral sites in spinel ferrites, Gd ions occupy the octahedral sites, as confirmed by the Rietveld analysis. The decrease in Fe occupancies in octahedral sites and the corresponding increase in Gd occupancies imply that Gd ions are properly substituted in octahedral sites. Some Fe and Mn ions are missing from tetrahedral and octahedral sites after Gd substitution.

This is due to the conversion of some Fe^{3+} ions into Fe^{2+} ions and Mn^{2+} to Mn^{3+}, which keeps charge neutrality in the system.

The ionic radii of tetrahedral and octahedral sites are calculated using the equation,

$$r_A = \left(u - \frac{1}{4}\right)a\sqrt{3} - r_o \qquad (12.a)$$

$$r_B = \left(\frac{5}{8} - u\right)a - r_o \qquad (12.b)$$

Here, r_A and r_B are the ionic radii of the atoms in tetrahedral and octahedral sites, respectively, a is the lattice constant, r_0 is the ionic radii of the oxygen atom and its value is 1.35 Å, and u is the oxygen position parameter obtained from refinement data [46,47]. Table 3.4 lists the calculated ionic radii of tetrahedral and octahedral sites. The ionic radii of the octahedral site are found to be larger than the ionic radii of the tetrahedral site because the octahedral sites contain more Mn/Fe ions or both [48]. The ionic radii of the tetrahedral and octahedral sites change with Gd substitution, which is due to the fact that Gd substitution changes the occupancies of Fe and Mn ions in the octahedral and tetrahedral sites, which alters the ionic radii of the corresponding sites. At x=0.02, the decrease in ionic radii in tetrahedral sites is due to the high missing of Fe and Mn ions, while the increase in octahedral sites is due to Fe transfer into Octahedral sites. Similarly, at x=0.04, the tetrahedral and octahedral ionic radii increase and decrease due to Fe transfer and missing in the tetrahedral and octahedral sites, respectively.

A space occurs between adjacent Fe and Mn ions in both tetrahedral and octahedral sites, and this space is known as the hopping length or jump length of magnetic ions. The hopping lengths of tetrahedral and octahedral sites are estimated using the following relations [49] and are shown in table 3.4.

$$L_A = \frac{a\sqrt{3}}{4} \qquad (13.a)$$

$$L_B = \frac{a\sqrt{2}}{4} \qquad (13.b)$$

Where L_A is the tetrahedral hopping length of magnetic ions in spinel ferrites and L_B is the octahedral hopping length. L_A and L_B of $MnFe_2O_4$ are found to increase with Gd substitution in Fe sites. The substitution of larger Gd^{3+} ions for smaller Fe^{3+} ions

increases the space between adjacent Fe and Mn ions, thus it increases the hopping length.

Table 3.4 Oxygen position parameter, ionic radii and hopping length of tetrahedral and octahedral site of MnFe$_{2-x}$Gd$_x$O$_4$ (x = 0.00, 0.02, 0.04)

Composition	U^{3m}	U^{43m}	Tetrahedral site		Octahedral site	
			r$_A$	L$_A$	r$_B$	L$_B$
0.00	0.2464	0.3714	0.4046	3.6184	0.7694	2.9544
0.02	0.2421	0.3671	0.3434	3.6199	0.8061	2.9556
0.04	0.2467	0.3717	0.4104	3.6200	0.7675	2.9558
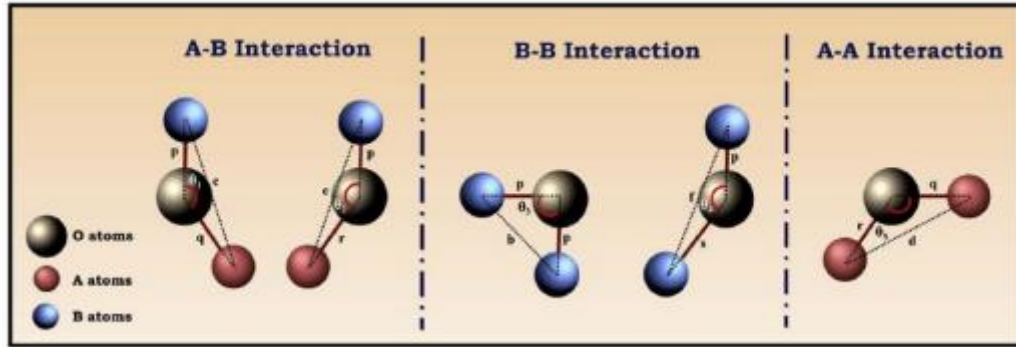
Figure 3.5 Pictorial representation of inter ionic distances of AB$_2$O$_4$ compound [51]

Magnetic interactions in spinel ferrites are classified into three types: A-A interactions, B-B interactions, and A-B interactions. The strength of these magnetic interactions is largely depended by bond length formed between metal cations and anions. The magnetic interactions in the material are strengthened by decreasing bond length [50]. The interionic distances are calculated to study the variation of bond length with respect to Gd substitution. The expressions for interionic distances in three magnetic interactions are given as [49],

$$p = a\left(\frac{5}{8} - u\right) \qquad (14.a)$$

$$q = a\sqrt{3}\left(u - \frac{1}{4}\right) \qquad (14.b)$$

$$r = a\sqrt{11}\left(u - \frac{1}{4}\right) \qquad (14.c)$$

$$s = a\sqrt{3}\left(\frac{u}{3} + \frac{1}{8}\right) \qquad \text{(14.d)}$$

$$b = \sqrt{2}\left(\frac{a}{4}\right) \qquad \text{(14.e)}$$

$$c = \sqrt{11}\left(\frac{a}{8}\right) \qquad \text{(14.f)}$$

$$d = \sqrt{3}\left(\frac{a}{4}\right) \qquad \text{(14.g)}$$

$$e = \sqrt{3}\left(\frac{3a}{8}\right) \qquad \text{(14.h)}$$

$$f = \sqrt{6}\left(\frac{a}{4}\right) \qquad \text{(14.i)}$$

Table 3.5 summarises the calculated interionic distances. The interionic distances are indirectly proportional to magnetic interactions like A-B interaction, B-B interaction and A-A interaction in the system. The interionic distances between cations for all interactions are found to increase with Gd substitution in Fe sites. However, the interionic distances between cation and anion shows an anomalous variation with Gd substitution. At $x = 0.02$ Gd content, the interionic distances between cation and anion get decrease except for the 'p'. But in the case of $x = 0.04$ Gd substitution, the 'p' value gets decreased and others get increased. It indicates that one of the interionic distances between cations corresponds to A-B, B-B and A-A interactions is decreases. Meanwhile, cation-anion interionic distances can enhance the magnetic interactions in the material. This anomalous behaviour may be due to the substitution effects of Gd ions which exhibit higher magnetic moments and larger ionic radii.

Table 3.5 Interatomic Bond length of $MnFe_{2-x}Gd_xO_4$ (x = 0.00, 0.02, 0.04)

x	Interionic Distances (cation-anion) in Å				Interionic Distances (cation-cation) in Å				
	p	q	r	s	b	c	d	e	f
0.00	2.1194	1.7566	3.3637	3.6008	2.9543	3.4643	3.6183	5.4275	5.1171
0.02	2.1561	1.6954	3.2465	3.5817	2.9556	3.4658	3.6199	5.4298	5.1193
0.04	2.1175	1.7625	3.3750	3.6042	2.9558	3.4659	3.6200	5.4301	5.1195

3.3 Optical studies

UV-Visible spectroscopy is a widely known method for investigating the optical properties of samples in the ultraviolet-visible range. The reflectance spectrum of pristine and Gd^{3+} substituted $MnFe_2O_4$ in the wavelength range 200-2500 nm is shown in Figure 3.4. From the figure, it is seen that the reflectance of both pristine and Gd^{3+} substituted $MnFe_2O_4$ increases with wavelength. The reflectance of pristine $MnFe_2O_4$ increases with Gd^{3+} substitution, indicating the formation of localised states between the conduction band and the valence band during the inclusion of Gd ions in Fe sites [52].
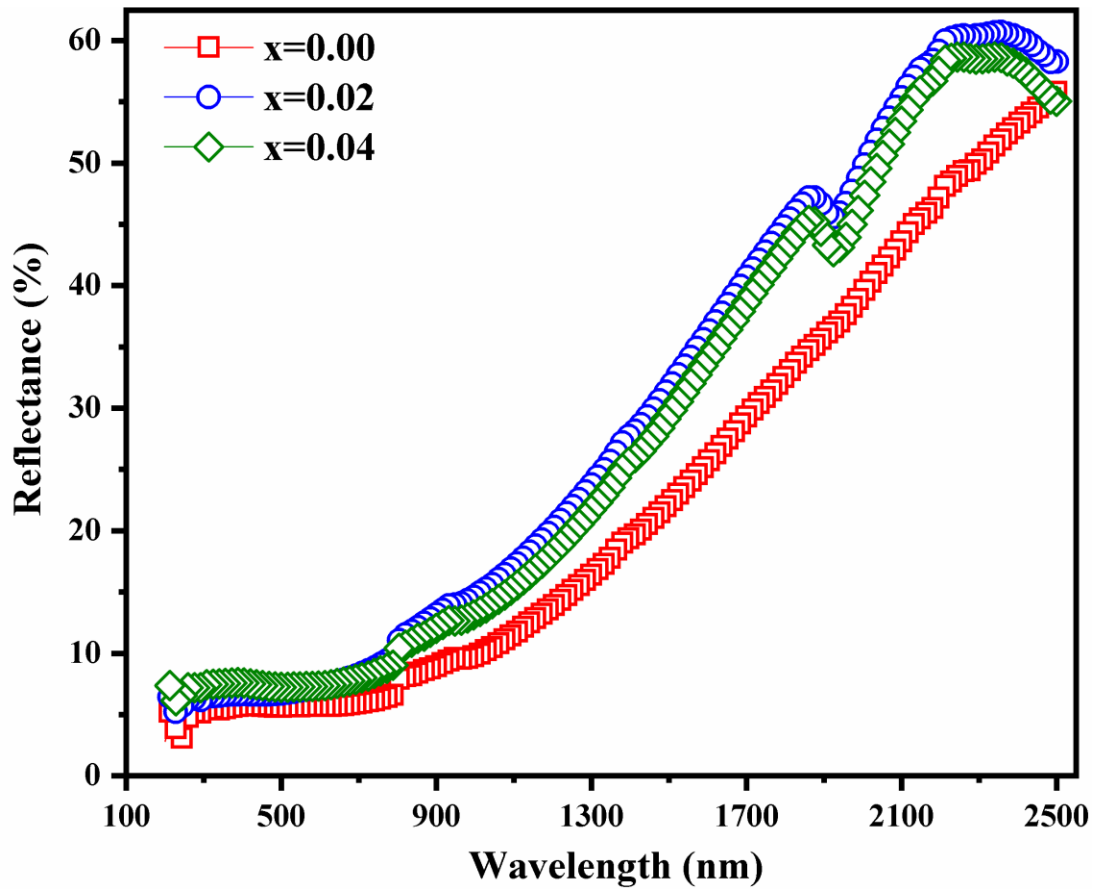
Figure 3.6 Reflectance spectrum of MnFe$_{2-x}$Gd$_x$O$_4$ (x = 0.00, 0.02, 0.04)

Kubelka-Munk function (F[R]) is used to estimate the optical band gap of the samples.

$$F(R_\infty) = \frac{(1-R_\infty)^2}{2R_\infty} \qquad (15)$$

Here R is the reflectance [53]. The bandgap energy calculated using tauc plot relation as,

$$F(R_\infty)h\upsilon = A\left(h\upsilon - E_g\right)^n \qquad (16)$$

Where hυ is the incident photon energy, A is the proportionality constant, E_g is the band gap energy of the material and n is the type of electronic transition that occurred in the material. A graph is plotted between $(\alpha h\vartheta)^{\frac{1}{n}}$ and photon energy hυ for different values of n to determine the optical band gap. If the plot shows a linear part for n = ½, the type of transition will be direct allowed transition. For n = 2, 3/2, 3, the type of transition will be indirect, forbidden direct, and forbidden indirect.

Both pristine and Gd substituted $MnFe_2O_4$, agreed on the tauc relation at n = 1/2 for the direct allowed transition. The plot of $[F(R_\infty)h\vartheta]^2$ vs photon energy for $MnFe_{2-x}Gd_xO_4$ is shown in figure 3.7. With Gd^{3+} substitution in Fe sites, the optical band gap of $MnFe_2O_4$ decreases. This is because localised states exist between the conduction and valence bands [54]. These localised states are caused by oxygen vacancies in the $MnFe_2O_4$ ensemble. Furthermore, substitution with Gd^{3+} produces some 4f energy states close to the conduction band, resulting in a narrowing of the band gap [51]. These localised states form shallow defect bands between the conduction and valence bands, trapping excited electrons and preventing direct electron transitions between the conduction and valence bands. This defect state is associated with the urbach energy of the sample. The relation used for calculating the Urbach energy is given below,

$$\alpha = \alpha_0 exp\left(\frac{h\upsilon}{E_u}\right) \qquad (17)$$

Where α is the absorption coefficient, E_u is the Urbach energy and hυ is the incident photon energy [55]. For powder samples, the kubelka-munk function can be used to replace the absorption coefficient. Figure 3.8 depicts the graph of ln F(R) as a function of photon energy for $MnFe_{2-x}Gd_xO_4$ (x = 0.00, 0.02, 0.04). The Urbach energy of the samples is determined by taking the reciprocal of the slope of these straight line graphs. It is found that the Urbach energy of $MnFe_2O_4$ increases with Gd^{3+} substitution in Fe sites, as shown in table 3.6. The creation of 4f states of Gd^{3+} ions near the conduction band is responsible for the increasing Urbach energy. This increase in Urbach energy is also related to the crystallinity of $MnFe_2O_4$, which decreases with Gd substitution and has a high structural disorder, as previously confirmed by XRD analysis. It has been found that urbach energy increases as the optical band gap decreases. Thus there exists an indirect relation between Urbach energy and band gap.
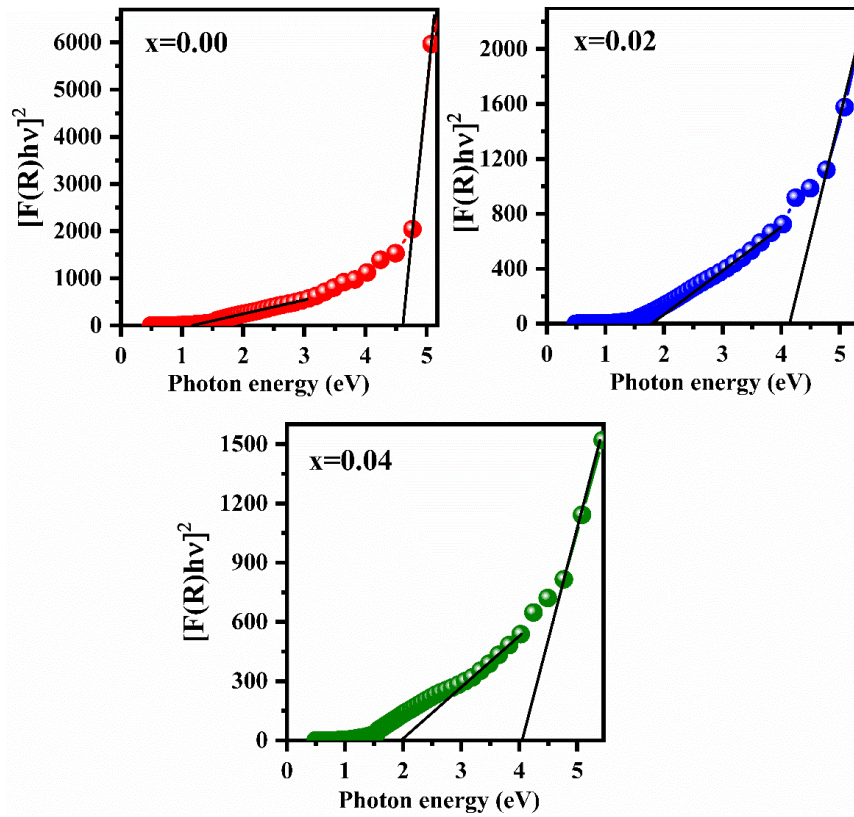
Figure 3.7 Estimation of Direct and Defect Band Gap of MnFe$_{2-x}$Gd$_x$O$_4$ (x = 0.00, 0.02, 0.04) using K-M function
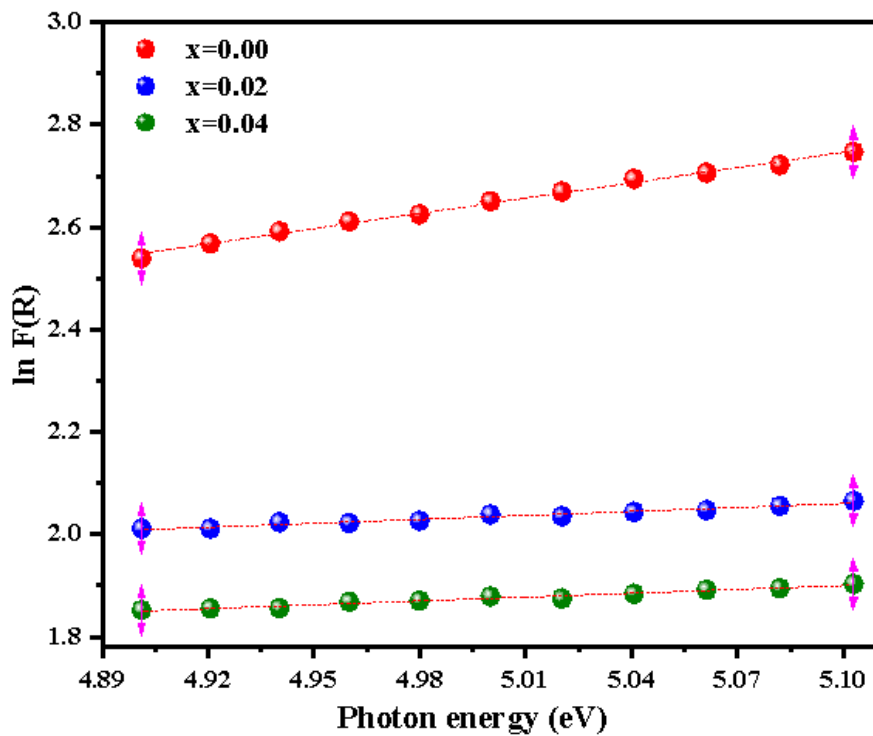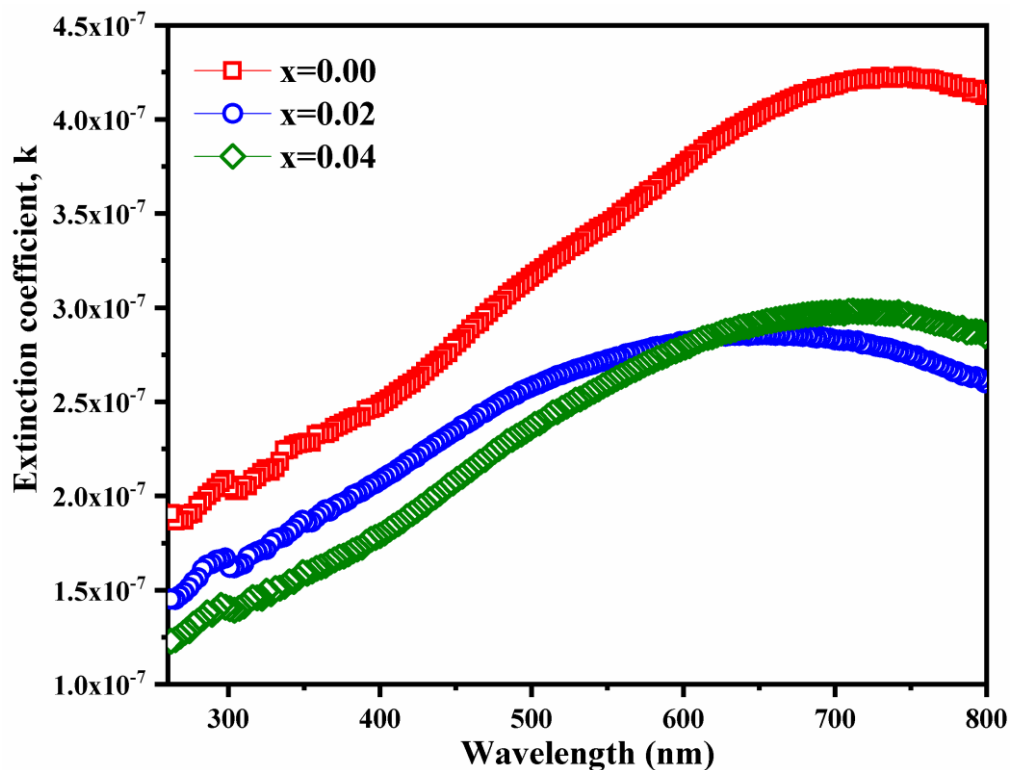

Figure 3.8 Urbach's Plot of MnFe$_{2-x}$Gd$_x$O$_4$ (x = 0.00, 0.02, 0.04)

Table 3.6 Band gap and Urbach energy of MnFe$_{2-x}$Gd$_x$O$_4$ (x = 0.00, 0.02, 0.04)

| Composition	Direct band gap	Defect band gap	Urbach energy
0.00	4.61	1.17	1.01
0.02	4.14	1.78	3.89
0.04	4.05	1.96	3.997

The refractive index and extinction coefficient are calculated to determine the optical performance of the material. The extinction coefficient is a measurement of how strongly a material absorbs light at a specific wavelength. Figure 3.9 depicts the variation of the extinction coefficient of pristine and Gd^{3+} substituted MnFe$_2$O$_4$ with respect to wavelength. It can be seen that the extinction coefficient of pristine MnFe$_2$O$_4$ increases with increasing wavelength, reaches its maximum value around 700 nm, and then decreases with increasing wavelength. The extinction coefficient exhibits similar behaviour with Gd^{3+} substitution, but has a lower value when compared to pristine MnFe$_2$O$_4$. This indicates that Gd^{3+} substituted MnFe$_2$O$_4$ exhibits low optical losses due to absorptions, which is clearly related to the material's optical quality.

Figure 3.9 Variation of extinction coefficient of MnFe$_{2-x}$Gd$_x$O$_4$ (x = 0.00, 0.02, 0.04) with Wavelength

Figure 3.10 shows the variation of refractive index with respect to wavelength variation for pristine and Gd substituted $MnFe_2O_4$. The refractive indices of pristine and Gd substituted $MnFe_2O_4$ exhibit normal dispersion behaviour. This is due to light energy dispersion at various interstitial levels. When compared to pristine $MnFe_2O_4$, Gd substituted $MnFe_2O_4$ has a higher refractive index. The refractive index is heavily influenced by the electronic polarizability of ions as well as the local field within the material. This higher refractive index value is mainly due to an increase in polarizability induced by the larger ionic radii of Gd ions, which causes structural distortion in $MnFe_2O_4$.
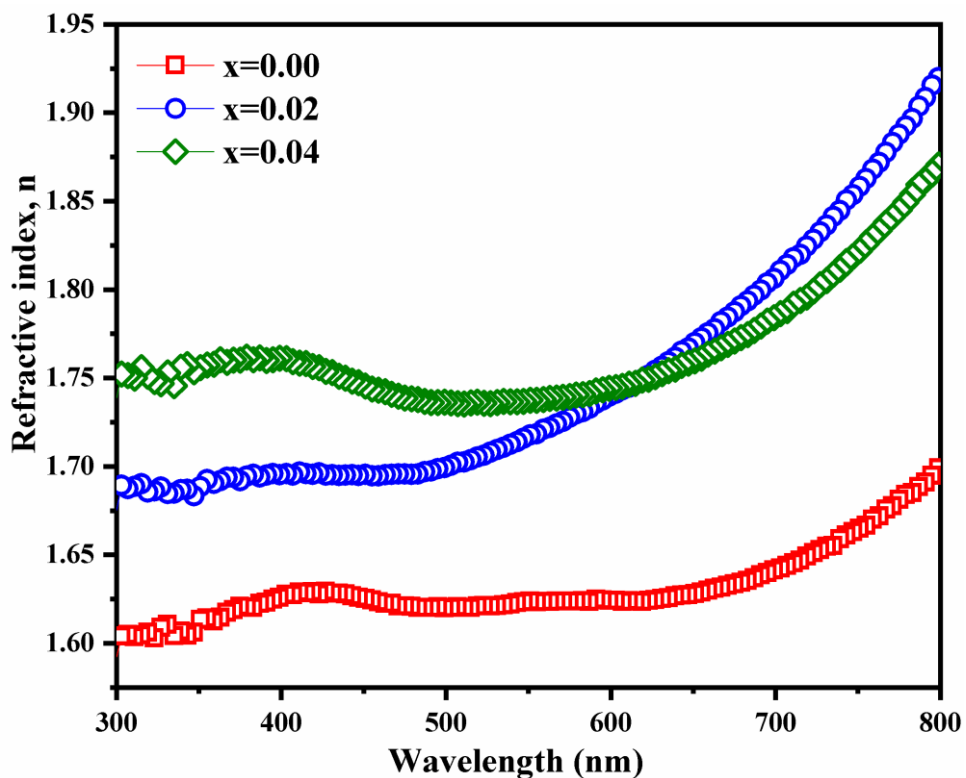

Figure 3.10 Evolution of Refractive index of $MnFe_{2-x}Gd_xO_4$ (x = 0.00, 0.02, 0.04) with wavelength

To investigate the dispersion behaviour of the refractive index, Wemple and DiDominica single oscillator model is used to investigate the dispersion behaviour of the refractive index. According to the Wemple and DiDominica model, refractive index dispersion was caused primarily by interband optical transitions in the material. The dispersion parameters of $MnFe_{2-x}Gd_xO_4$ (x = 0.00, 0.02, 0.04) are calculated using the equation given as:

$$n^2 - 1 = \frac{E_d E_o}{E_0^2 - (hv)^2} \qquad (18)$$

Here E_d is the dispersion energy or oscillator strength and E_0 is the oscillator energy. E_d give information about inter-band optical transition and E_0 describes the average energy gap. The dispersion parameters of $MnFe_{2-x}Gd_xO_4$ (x = 0.00, 0.02, 0.04) are extracted from the graph between $(n^2-1)^{-1}$ and $(hv)^2$. E_0 and E_d can be determined directly from the slope $(E_0 E_d)^{-1}$ and the intercept E_0/E_d of the graph. The estimated values of E_0 and E_d are tabulated in table 3.7.
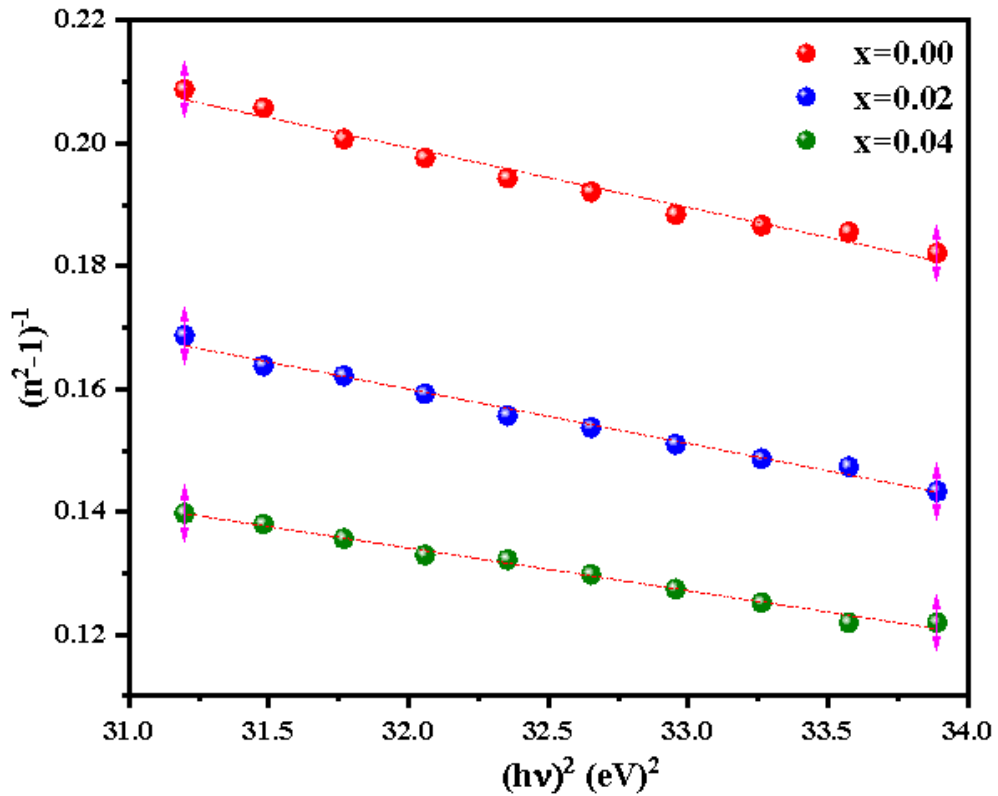
Figure 3.11 $(n^2-1)^{-1}$ and $(hv)^2$ graph of $MnFe_{2-x}Gd_xO_4$ (x = 0.00, 0.02, 0.04)

With Gd substitution, the dispersion energy increases while the oscillator energy decreases. This increasing dispersion energy suggests that Gd substitution promotes inter-band formation between the conduction and valence bands. This reveals that the inclusion of Gd improves the interband optical transition in $MnFe_2O_4$. The optical band gap of the material is directly correlated with the E_0 oscillator energy, as expressed by,

$$E_0 = \gamma E_g \qquad (19)$$

Here γ is the coefficient of proportionality. It has been found that oscillator energy, like the optical band gap, decreases with Gd substitution, implying that the bond strength of $MnFe_2O_4$ decreases with Gd substitution.

Figure 3.7 Dispersion parameters of $MnFe_{2-x}Gd_xO_4$ (x = 0.00, 0.02, 0.04)

Composition, x	E_d (eV)	E_0 (eV)	E_g (eV)	γ
0.00	14.18	7.24	4.61	1.57
0.02	15.97	7.08	4.14	1.71
0.04	20.07	7.16	4.05	1.77

To investigate the influence of free charge carriers, lattice dielectric constant (ε_L) and free carrier concentration within effective mass (N/m*) are calculated using,

$$n^2 = \varepsilon_L - \left(\frac{e^2}{4\pi c^2 \varepsilon_0}\right)\left(\frac{N}{m*}\right)\lambda^2 \qquad (19)$$

Here, e is the elementary charge, ε_0 is the absolute permittivity in free space. The intercept and slope of the plot n^2 vs λ^2 can be used to calculate the values of ε_L and N/m*. The plot between n^2 and λ^2 of $MnFe_{2-x}Gd_xO4$ (x = 0.00, 0.02, 0.04) is shown in the figure 3.12 and values estimated are tabulated in table 3.8.
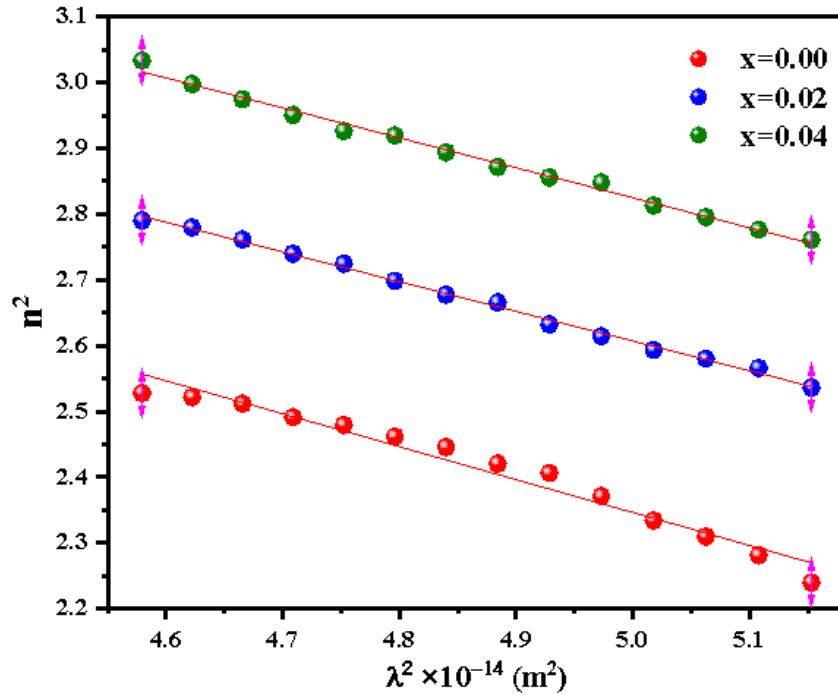
Figure 3.12 n^2 and λ^2 graph of $MnFe_{2-x}Gd_xO4$ (x = 0.00, 0.02, 0.04)

Both the lattice dielectric constant and N/m* are found to increase with Gd substitution. This enhancement is mainly due to the larger ionic radii of Gd. Substitution with Gd ions create Fe^{2+} and Mn^{3+} ions in the ensemble which increases the number of free charge carriers in the system and enhances the dielectric constant.

To investigate the effect of bound carriers in the material, the Moss model is used, which suggests that the effect of free charge carrier concentration is negligible in the high frequency region. The motion of bound carriers in the material produces a high frequency dielectric constant that is related to the refractive index. The single term Sellmeier oscillator equations that connect the static dielectric constant and refractive index are as follows:

$$\frac{n_s^2 - 1}{n^2 - 1} = 1 - \left(\frac{\lambda_0}{\lambda}\right)^2 \qquad (20)$$

Where, λ_o is the inter-band oscillator wavelength and n_s represents a static refractive index of the material. $\varepsilon_s = n_s^2$ is the static dielectric constant. Static refractive index and inter band oscillator wavelength are determined from slope and intercept of $(n^2-1)^{-1}$ versus λ^{-2} plot. The graph between $(n^2-1)^{-1}$ versus λ^{-2} of $MnFe_{2-x}Gd_xO_4$ (x = 0.00, 0.02, 0.04) is shown in the figure 3.13 and the values of ε_s and λ_o obtained are tabulated in table 3.8.
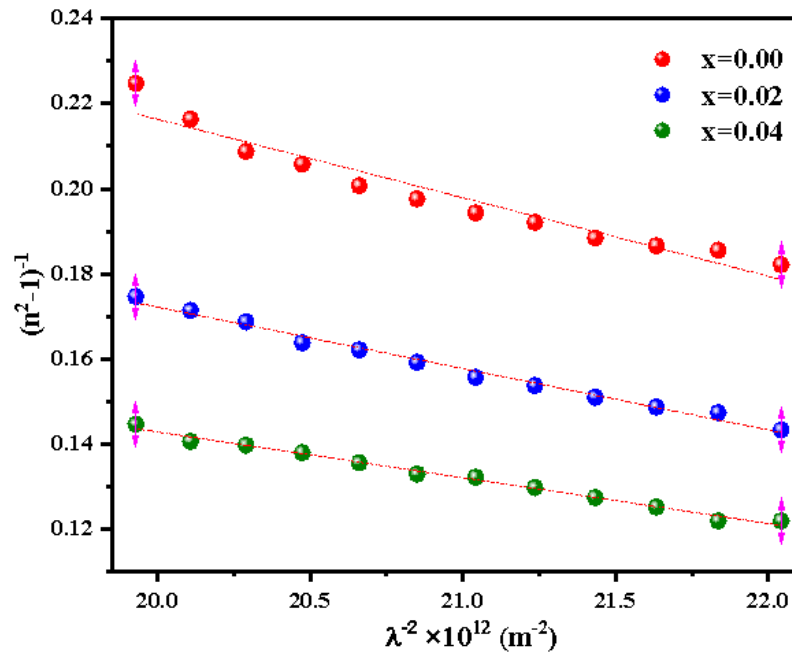

Figure 3.13 $(n^2-1)^{-1}$ and λ^{-2} graph of $MnFe_{2-x}Gd_xO_4$ (x = 0.00, 0.02, 0.04)

It is observed that the high frequency dielectric constant increases with Gd substitution in Fe sites, implying that bound electrons attracted to the nucleus influence the dispersion of the refractive index and help to improve the material's dielectric properties. The lattice dielectric constant (ε_L) of $MnFe_{2-x}Gd_xO_4$ (x = 0.00, 0.02, 0.04) is greater than the high frequency dielectric constant (ε_s) , indicating that the free charge carrier contribution has a greater impact on the dispersion of the refractive index in $MnFe_{2-x}Gd_xO4$ (x = 0.00, 0.02, 0.04) than the bound carrier contribution.

Table 3.8 Lattice dielectric constant, free charge carrier concentration and threshold wavelength of $MnFe_{2-x}Gd_xO_4$ (x = 0.00, 0.02, 0.04)

Composition, x	ε_L	$N/M^*\ (\times 10^{59})$	ε_∞	λ_0 (nm)
0.00	4.85	1.62	2.70	178
0.02	4.87	1.80	3.17	177
0.04	5.10	1.79	3.79	173

The complex dielectric constant is a critical quantity in the design of high-efficiency optoelectronic and magneto-optic devices. The complex dielectric function can be expressed as follows:

$$\varepsilon^* = \varepsilon_{real} + i\varepsilon_{imaginary} \qquad (21)$$

where, ε_{real} represents the real dielectric permittivity of material which gives the dispersion rate of an incident photon in the sample $\varepsilon_{imaginary}$ represents how the sample absorbs energy from an electric field due to dipole motion throughout the uv-visible region. The real and imaginary dielectric constants can calculated by given equations,

$$\varepsilon_1 = n^2 - k^2 \qquad (22.a)$$

$$\varepsilon_2 = 2nk \qquad (22.b)$$

where ε_1 & ε_2 are the dielectric constants of real and imaginary parts respectively. Figure 3.14 shows the variation of real dielectric permittivity of $MnFe_{2-x}Gd_xO_4$ (x = 0.00, 0.02, 0.04) as a function of incident photon energy. It is found that Gd substitution in Fe sites increases the real dielectric permittivity of $MnFe_2O_4$. To maintain charge neutrality, Gd ion substitution produces more Fe^{2+} and Mn^{3+} ions in the lattice, which improves the

electron hopping rate between Fe^{2+} and Fe^{3+} ions and hole hopping between Mn^{3+} and Mn^{2+} ions. Furthermore, substitution with larger Gd ions causes a lattice distortion within the crystal lattice, which increases electric polarisation. The increase in dielectric permittivity within the material is caused by an increase in electron hopping rate and electric polarisation of the material.
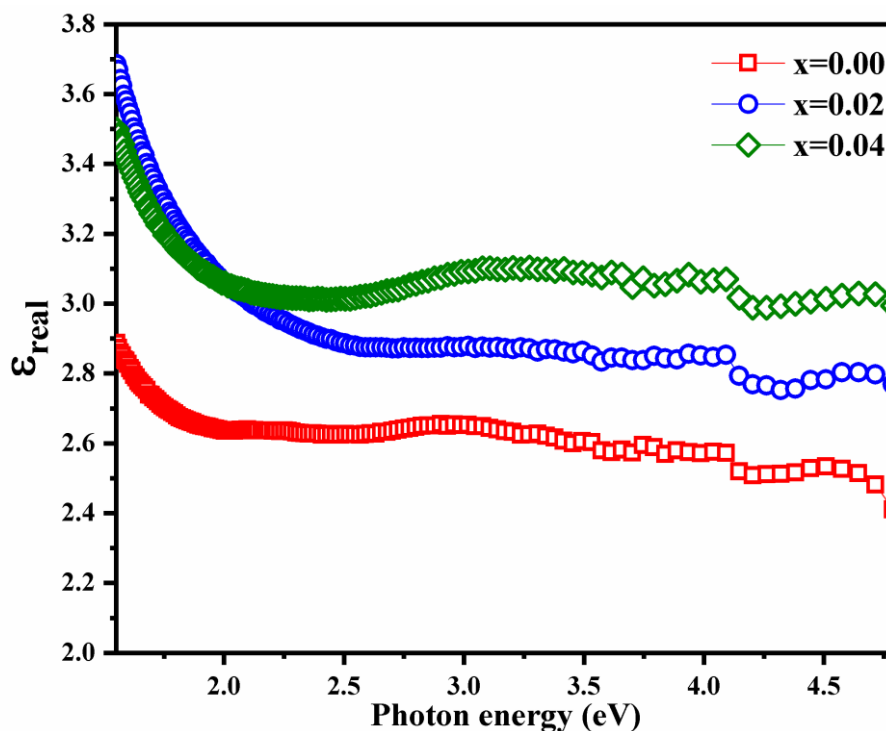
Figure 3.14 Variation of ε_{real} of $MnFe_{2-x}Gd_xO_4$ (x = 0.00, 0.02, 0.04) with photon energy.

The variation of imaginary dielectric permittivity as a function of incident photon energy in pristine and Gd substituted $MnFe_2O_4$ is shown in the figure 3.15. It is found that substitution with Gd ions decreases the energy loss of $MnFe_2O_4$ in the uv–visible region. Substitution with Gd ions creates more Fe^{2+} and Mn^{2+} ions and enhances the electron hopping of Fe ions in $MnFe_2O_4$. This increase in electron hopping reduces the energy loss in the material during the absorption process. According to the results of both real and imaginary dielectric permittivity, substitution with Gd ions in Fe sites improves the dielectric properties of $MnFe_2O_4$ at higher frequency regions.
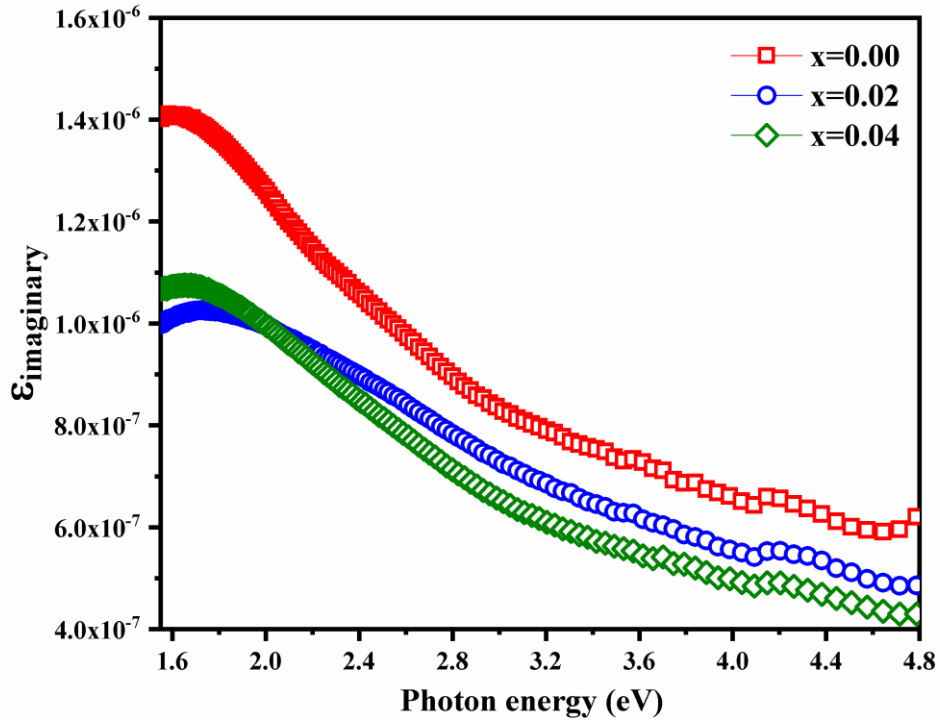
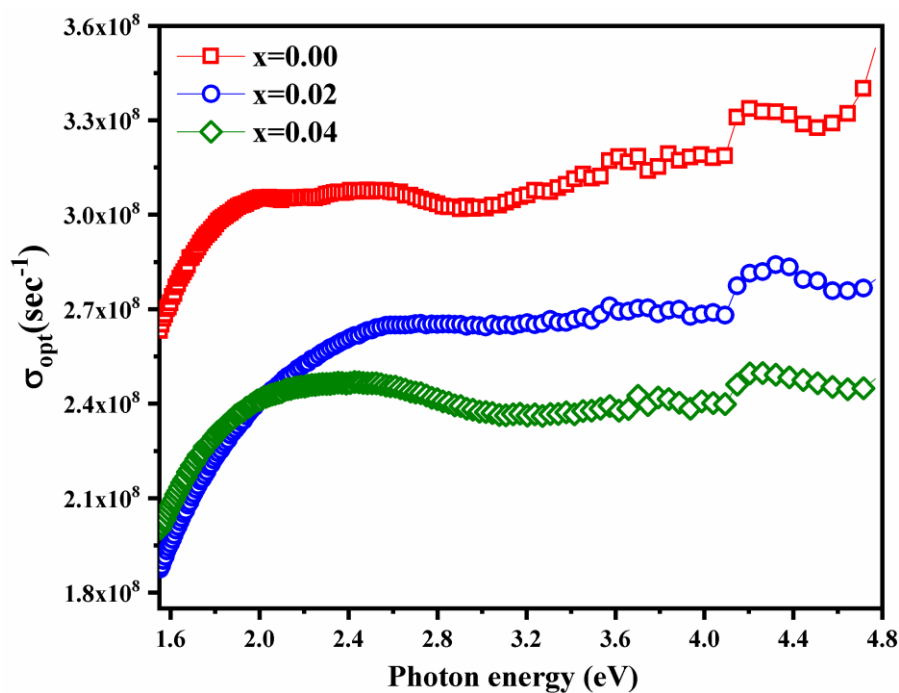**Figure 3.15 Variation of $\varepsilon_{imaginary}$ of MnFe$_{2-x}$Gd$_x$O$_4$ (x = 0.00, 0.02, 0.04) with photon energy.**

Variation of optical conductivity of pristine and Gd substituted MnFe$_2$O$_4$ with respect to photon energy is shown in the figure 3.16. The optical conductivity of materials is calculated using equation,

$$\sigma_{opt} = \frac{F(R)nc}{4\pi} \qquad (23.a)$$

$$\sigma_{elec} = \frac{2\lambda\sigma_{opt}}{F(R)} \qquad (23.b)$$

The optical conductivity is found to increase with photon energy. It is because higher photon energy results from higher electron excitation due to higher absorption values. The optical conductivity of Gd substitution is slightly lower than that of pristine one. The presence of a large number of localised states between the conduction and valence bands contributes to the decrease in optical conductivity. These localised states cause charge carriers to trap between the conduction and valence bands, resulting in incomplete charge carrier transfer in the UV - visible region. Since the incomplete transfer of charge carriers reduces phonon conduction in the material, optical conductivity decreases with increasing Gd content.

Figure 3.16 Variation of optical conductivity of MnFe$_{2-x}$Gd$_x$O$_4$ (x = 0.00, 0.02, 0.04) with photon energy.
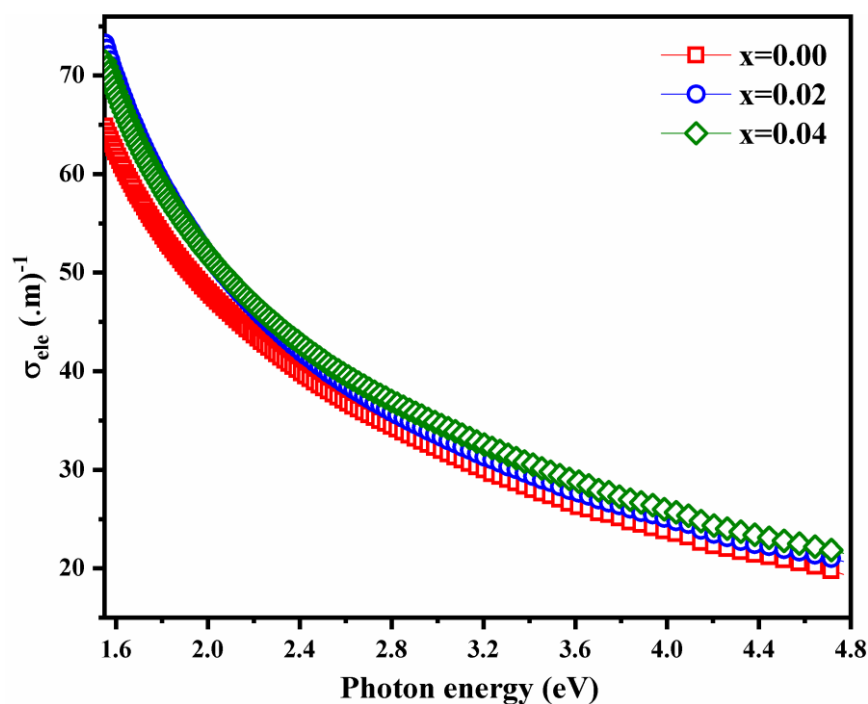
Figure 3.17 Variation of electrical conductivity of MnFe$_{2-x}$Gd$_x$O$_4$ (x = 0.00, 0.02, 0.04) with photon energy.

Variation of electrical conductivity of MnFe$_{2-x}$Gd$_x$O4 (x = 0.00, 0.02, 0.04) is shown in the figure 3.17 in the uv-visible region. It is observed that the electrical conductivity of

$MnFe_{2-x}Gd_xO_4$ (x = 0.00, 0.02, 0.04) decreases as incident photon energy increases. Electrical conduction is very low in the high photon energy region due to the low rate of hopping between Fe^{2+}-Fe^{3+} and Mn^{3+}-Mn^{2+} ions. Since optical conductivity is nearly 10^7 times greater than electrical conductivity, photon conduction rather than electrical conduction is the dominant mechanism in the UV-visible region. Electrical conduction is found to increase with Gd substitution in the Fe sites of $MnFe_2O_4$. As previously stated, substitution with Gd ions in $MnFe_2O_4$ Fe sites results in a large number of Fe^{2+} and Mn^{2+} ions in the lattice. With increasing Gd content, this enrichment of Fe^{2+} and Mn^{2+} ions improves the hopping of Fe^{2+} - Fe^{3+} ions/ Mn^{3+} -Mn^{2+} and increases the electrical conductivity of $MnFe_2O_4$.

3.4 Dielectric study

The dielectric spectroscopy of $MnFe_{2-x}Gd_xO4$ (x = 0.00, 0.02, 0.04) was studied at frequencies ranging from 500Hz to 1 MHz. The dielectric permittivity is calculated using the equation,

$$\varepsilon = \frac{Ct}{\varepsilon_0 A} \qquad (24)$$

Where C, t, A, and ε_0 are capacitance, sample thickness, sample area, and absolute permittivity of free space, respectively. Figure 3.18 shows the variation of dielectric permittivity as a function of frequency for $MnFe_{2-x}Gd_xO4$ (x = 0.00, 0.02, 0.04) at room temperature. The dielectric permittivity of $MnFe_2O_4$ decreases with frequency and remains constant at high frequencies. This is mainly due to Maxwell-Wagner Polarization [53]. Which is based on the fact that a dielectric medium consists of two layers separated by resistive grain boundaries. When an external electric field is applied, charges on the grains are displaced and accumulated at grain boundaries, causing them to behave as an electric dipole and produce electric polarization. At low frequencies, electrons hop and gather at boundaries, resulting in electric polarisation. The probability of electron gathering decreases as frequency increases, as does polarisation, which results in a decrease in dielectric permittivity. Beyond a certain frequency, charge carriers are unable to follow in the direction of a fast changing alternating field, which causes the hopping of charge carriers to lag behind the applied field and results in a decrease in electric polarisation.

With Gd substitution dielectric permittivity increases. The structural distortion caused by the substitution with larger Gd ions leads to an increase in dielectric permittivity with Gd substitution. This structural distortion is occurred by the deviation of the oxygen position parameter from their ideal position which destroys the centrosymmetric nature of octahedrons, which induces polarization in the system. Besides structural distortion, an increase in free charge carrier concentration enhances electron hopping between Fe^{2+}–Fe^{3+} ions, and hole hopping of Mn^{3+}–Mn^{2+} ions. Rietveld refinement of XRD patterns has already confirmed the shifting of the oxygen position parameter and formation of excess Fe^{2+} and Mn^{2+}, and the evidence for the excess free charge carrier concentration was supplemented by the optical properties of $MnFe_{2-x}Gd_xO_4$ (x = 0.00, 0.02, 0.04). The formation of excess Fe^{2+} and Mn^{2+} is confirmed by the Rietveld refinement, which enriches the hopping mechanism and thus results in high polarization.
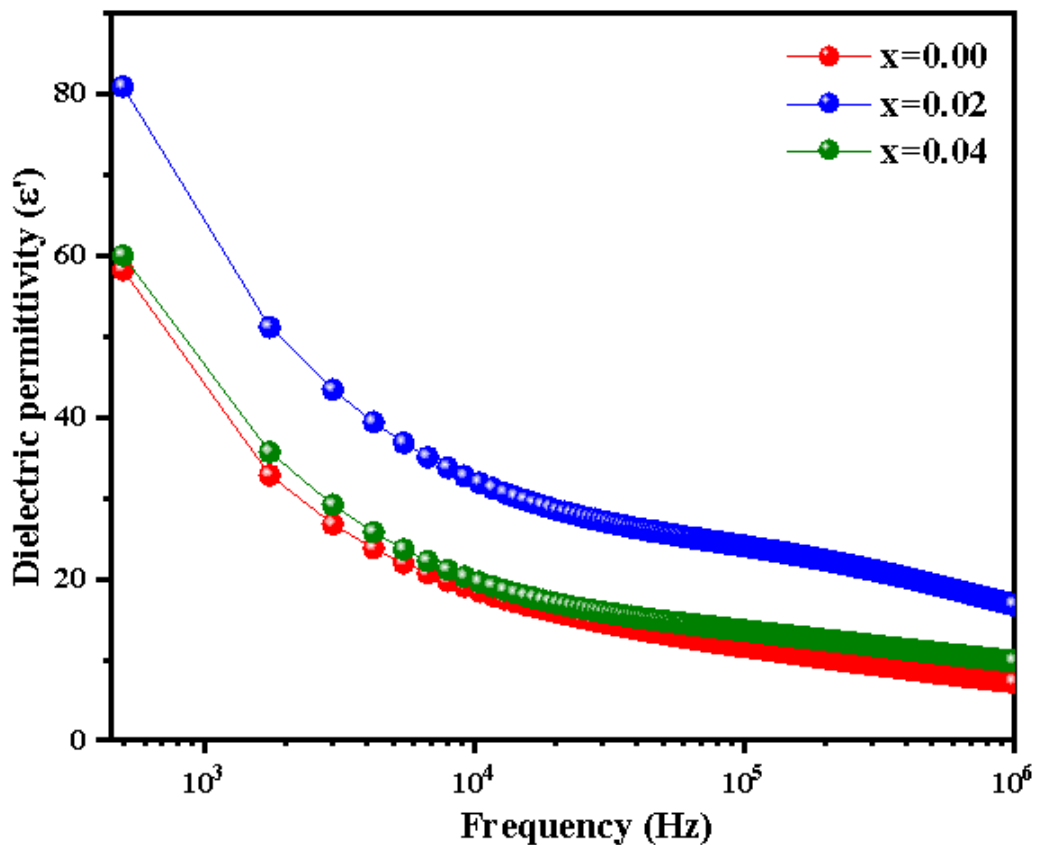
Figure 3.18 The frequency response of dielectric permittivity of MnFe₂₋ₓGdₓO₄ (x = 0.00, 0.02, 0.04) at room temperature.

Variation of loss tangent with respect to frequency for $MnFe_{2-x}Gd_xO_4$ (x = 0.00, 0.02, 0.04) to the range 500 Hz to 1 MHz is shown in the figure 3.19. The loss tangent was primarily caused by the system's incomplete polarisation. When compared to pristine $MnFe_2O_4$, the loss tangent of $MnFe_{2-x}Gd_xO_4$ (x = 0.02, 0.04) exhibits a lower value. Tangent loss is also higher in the low frequency region due to the lower energy, which is unable to activate the hopping of Fe^{2+}-Fe^{3+} and Mn^{3+}-Mn^{2+} ions across resistive grain boundaries, resulting in incomplete polarisation and increasing loss tangent. With increasing frequency, the energy required for electron exchange decreases, resulting in a decrease in the dielectric loss factor. With Gd substitution, the tangent loss gets reduced and the minimum value of the tangent loss is obtained for x = 0.02. The increasing free charge carriers enhance the hopping rate of electron and hole hopping which reduces the tangent loss with Gd substitution
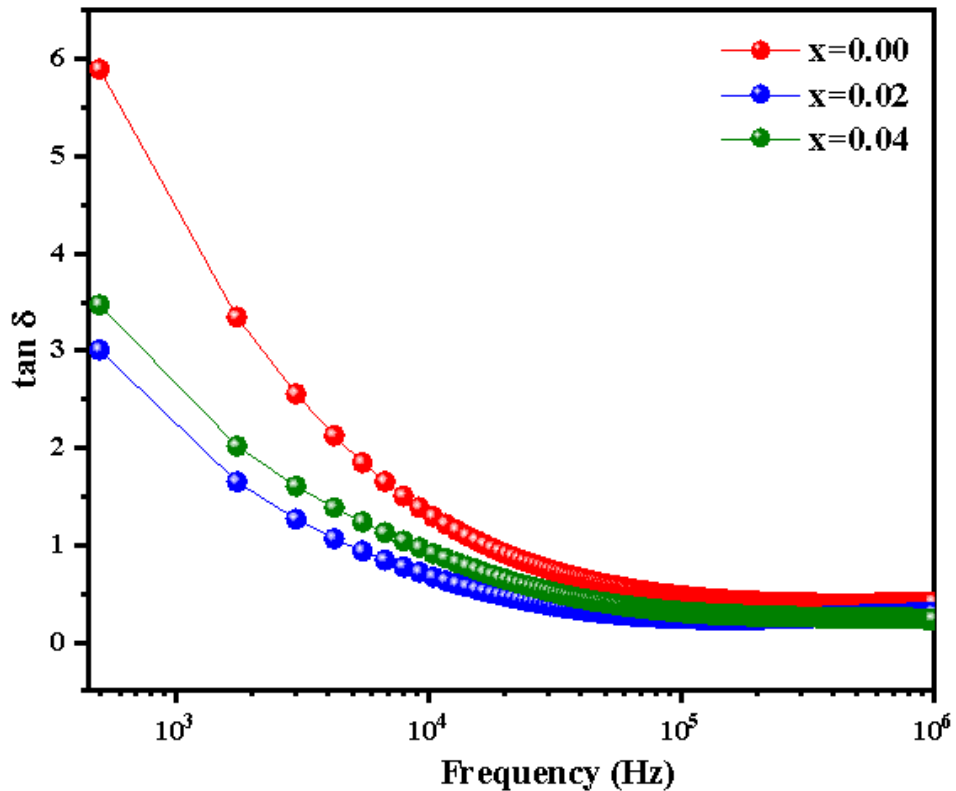
Figure 3.19 Dielectric loss factor (Tangent loss) as a function of frequency of $MnFe_{2-x}Gd_xO_4$ (x = 0.00, 0.02, 0.04) at room temperature

Chapter 5

Conclusions

Manganese spinel ferrites are a well-known material which exhibits high magnetic properties at room temperature and are used in various fields such as ferrofluids, electromagnetic interference suppression (EMIS), microwave absorption, batteries, sensors and supercapacitors. Single-phasic pristine and Gd substituted $MnFe_2O_4$ samples were prepared successfully via a sol-gel method. From Rietveld refinement of XRD patterns, it is confirmed that $MnFe_{2-x}Gd_xO_4$ (x =0.00, 0.02, 0.04) exhibit a spinel cubic structure with Fd-3m space group. Gadolinium substitution in Fe sites of $MnFe_2O_4$ increases the lattice constant and cell volume of the crystal lattice. It is due to the larger ionic radii of Gd^{3+} ions. Gd substitution in Fe sites increases the interionic distances between adjacent cations and it strongly depend on the magnetic interaction in the material.

Optical studies reveal that the direct band gap of $MnFe_2O_4$ was found to be decreasing with Gd substitution. This decrease in the band gap is due to the effect of localized states that occurred in the samples and it increases with Gd substitution which on further confirmed by Urbach energy variation. Dispersion energy and oscillatory energy reveals that Gd substitution promotes inter-band formation between the conduction and valance bands. Gd substitution in Fe sites reduces optical loss and increases the electronic polarizability of $MnFe_2O_4$. Real dielectric permittivity increases and imaginary dielectric permittivity decreases with Gd substitution in the terahertz frequency region. Lattice dielectric constant increases with Gd substitution due to the structural distortion that occurred in the material.

Dielectric spectroscopic methods were used to investigate the effect of Gd substitution on the dielectric behaviour of $MnFe_2O_4$ in the 500 Hz to 1 MHz region. Gd substituted samples showed a significant increase in dielectric permittivity. This increase in dielectric permittivity is caused by octahedral distortion occurring in the material due to the larger ionic radii of Gd ions and it is confirmed by evaluating oxygen position parameters. It is found that dielectric permittivity and oxygen position parameters exhibit a direct relation in Gd substituted $MnFe_2O_4$. An increase in electron hopping

between Fe^{2+}–Fe^{3+} ions, hole hopping of Mn^{3+}–Mn^{2+} ions and excess free charge carrier concentration also help to enhance the dielectric properties of the material.

Chapter 5

Future Scope of the Work

Magnetism and ferroelectricity are inevitable phenomena in technological areas due to their wide range of applications. It is very hard to coexist these properties in a single material due to their different origin of basis. In recent days, researchers have developed many routes to combine these properties in a single-phase material. The coexistence of these properties in a single-phase material will help to develop efficient sensors and memory devices in scientific and technological areas. Recent studies in $MnFe_2O_4$ with RE substitution have great attention due to the ability to enhance the magnetic and electrical properties of the parent material. In this work, we carried out preliminary studies such as substitution impact on the structural, electrical and optical properties of $MnFe_2O_4$. The enhancement of dielectric and optical properties with Gd substitution opens a window that which could be possible to coexist ferroelectricity and magnetism in single phase material. Therefore, a systematic study on magnetic and ferroelectric properties uncovers the mechanisms and effect of rare earth ions in the magnetic and electric properties of the material. In future, the memory devices manufactured by multiferroic materials must be million dollar business in technological areas.

References

[1] M.A. Wahab, Solid State Physics, Narosa Publishing House , 1999.

[2] Dipole Moment, (n.d.). https://ch301.cm.utexas.edu/imfs/#polar/dipole-moment.html (accessed August 29, 2022).

[3] Interfacial Polarization, (n.d.). https://www.sciencedirect.com/topics/engineering/interfacial-polarization#:~:text=The%20space%20charge%2C%20or%20interfacial,the%20interfaces%20between%20different%20materials. (accessed August 29, 2022).

[4] V. v. Jadhav, S.D. Shirsat, U.B. Tumberphale, R.S. Mane, Properties of ferrites, in: Spinel Ferrite Nanostructures for Energy Storage Devices, Elsevier, 2020: pp. 35–50. https://doi.org/10.1016/B978-0-12-819237-5.00003-1.

[5] T. Ejaz, Optimization of Split-Ring and Split-Ball Resonators for Effective Permittivity and Volume Fraction Extraction, 2017.

[6] A.J. Dekker, Solid State Physics, Macmillan, 1965.

[7] J.S. Galsin, Solid State Physics: An introduction to theory, Academics press , 2019.

[8] M. Amiri, M. Salavati-Niasari, A. Akbari, Magnetic nanocarriers: Evolution of spinel ferrites for medical applications, Adv Colloid Interface Sci. 265 (2019) 29–44. https://doi.org/10.1016/j.cis.2019.01.003.

[9] A. Moitra, S. Kim, S.-G. Kim, S.C. Erwin, Y.-K. Hong, J. Park, Defect formation energy and magnetic properties of aluminum-substituted M-type barium hexaferrite, Computational Condensed Matter. 1 (2014) 45–50. https://doi.org/10.1016/j.cocom.2014.11.001.

[10] A.B. Mapossa, W. Mhike, J.L. Adalima, S. Tichapondwa, Removal of Organic Dyes from Water and Wastewater Using Magnetic Ferrite-Based Titanium Oxide and Zinc Oxide Nanocomposites: A Review, Catalysts. 11 (2021) 1543. https://doi.org/10.3390/catal11121543.

[11] R.C. Pullar, Hexagonal ferrites: A review of the synthesis, properties and applications of hexaferrite ceramics, Prog Mater Sci. 57 (2012) 1191–1334. https://doi.org/10.1016/j.pmatsci.2012.04.001.

[12] A. Moitra, S. Kim, S.-G. Kim, S.C. Erwin, Y.-K. Hong, J. Park, Defect formation energy and magnetic properties of aluminum-substituted M-type barium hexaferrite, Computational Condensed Matter. 1 (2014) 45–50. https://doi.org/10.1016/j.cocom.2014.11.001.

[13] R. Valenzuela, Novel Applications of Ferrites, Physics Research International. 2012 (2012) 1–9. https://doi.org/10.1155/2012/591839.

[14] R. Nakamoto, B. Xu, C. Xu, H. Xu, L. Bellaiche, Properties of rare-earth iron garnets from first principles, Phys Rev B. 95 (2017) 024434. https://doi.org/10.1103/PhysRevB.95.024434.

[15] Gadolinium Orthoferrite – GdFeO3, (n.d.). https://www.chemtube3d.com/ss-gdfeo3/ (accessed August 29, 2022).

[16] S.F. Shaikh, M. Ubaidullah, R.S. Mane, A.M. Al-Enizi, Types, Synthesis methods and applications of ferrites, in: Spinel Ferrite Nanostructures for Energy Storage Devices, Elsevier, 2020: pp. 51–82. https://doi.org/10.1016/B978-0-12-819237-5.00004-3.

[17] T. Shanmugavel, S. Gokul Raj, G.R. Kumar, G. Rajarajan, Synthesis and Structural Analysis of Nanocrystalline MnFe2O4, Phys Procedia. 54 (2014) 159–163. https://doi.org/10.1016/j.phpro.2014.10.053.

[18] S. Ahmad, S. Ali, I. Ullah, M.S. Zobaer, A. Albakri, T. Muhammad, Synthesis and characterization of manganese ferrite from low grade manganese ore through solid state reaction route, Sci Rep. 11 (2021) 16190. https://doi.org/10.1038/s41598-021-95625-z.

[19] M. Goodarz Naseri, E. bin Saion, H.A. Ahangar, M. Hashim, A.H. Shaari, Synthesis and characterization of manganese ferrite nanoparticles by thermal treatment method, J Magn Magn Mater. 323 (2011) 1745–1749. https://doi.org/10.1016/j.jmmm.2011.01.016.

[20] E.C. Devi, I. Soibam, Effect of Zn doping on the structural, electrical and magnetic properties of MnFe2O4 nanoparticles, Indian Journal of Physics. 91 (2017) 861–867. https://doi.org/10.1007/s12648-017-0981-7.

[21] A. Mary Jacintha, V. Umapathy, P. Neeraja, S. Rex Jeya Rajkumar, Synthesis and comparative studies of MnFe2O4 nanoparticles with different natural polymers by sol–gel method: structural, morphological, optical, magnetic, catalytic and biological activities, J Nanostructure Chem. 7 (2017) 375–387. https://doi.org/10.1007/s40097-017-0248-z.

[22] B. Aslibeiki, P. Kameli, M.H. Ehsani, H. Salamati, G. Muscas, E. Agostinelli, V. Foglietti, S. Casciardi, D. Peddis, Solvothermal synthesis of MnFe2O4 nanoparticles: The role of polymer coating on morphology and magnetic properties, J Magn Magn Mater. 399 (2016) 236–244. https://doi.org/10.1016/j.jmmm.2015.09.081.

[23] J. Li, H. Yuan, G. Li, Y. Liu, J. Leng, Cation distribution dependence of magnetic properties of sol–gel prepared MnFe2O4 spinel ferrite nanoparticles, J Magn Magn Mater. 322 (2010) 3396–3400. https://doi.org/10.1016/j.jmmm.2010.06.035.

[24] S.V. Bhandare, R. Kumar, A.V. Anupama, H.K. Choudhary, V.M. Jali, B. Sahoo, Annealing temperature dependent structural and magnetic properties of MnFe 2 O 4 nanoparticles grown by sol-gel auto-combustion method, J Magn Magn Mater. 433 (2017) 29–34. https://doi.org/10.1016/j.jmmm.2017.02.040.

[25] T. Şimşek, S. Akansel, Ş. Özcan, A. Ceylan, Synthesis of MnFe2O4 nanocrystals by wet-milling under atmospheric conditions, Ceram Int. 40 (2014) 7953–7956. https://doi.org/10.1016/j.ceramint.2013.12.144.

[26] S. Chella, P. Kollu, E.V.P.R. Komarala, S. Doshi, M. Saranya, S. Felix, R. Ramachandran, P. Saravanan, V.L. Koneru, V. Venugopal, S.K. Jeong, A. Nirmala Grace, Solvothermal synthesis of MnFe2O4-graphene composite—Investigation of its adsorption and antimicrobial properties, Appl Surf Sci. 327 (2015) 27–36. https://doi.org/10.1016/j.apsusc.2014.11.096.

[27] M.A.S. Amulya, H.P. Nagaswarupa, M.R.A. Kumar, C.R. Ravikumar, K.B. Kusuma, Sonochemical synthesis of MnFe2O4 nanoparticles and their electrochemical and photocatalytic properties, Journal of Physics and Chemistry of Solids. 148 (2021) 109661. https://doi.org/10.1016/j.jpcs.2020.109661.

[28] L. Zhen, K. He, C.Y. Xu, W.Z. Shao, Synthesis and characterization of single-crystalline MnFe2O4 nanorods via a surfactant-free hydrothermal route, J Magn Magn Mater. 320 (2008) 2672–2675. https://doi.org/10.1016/j.jmmm.2008.05.034.

[29] P. Rivas, V. Sagredo, F. Rossi, C. Pernechele, M. Solzi, O. Pena, Structural, Magnetic, and Optical Characterization of MnFe2O4 Nanoparticles Synthesized Via Sol-Gel Method, IEEE Trans Magn. 49 (2013) 4568–4571. https://doi.org/10.1109/TMAG.2013.2262039.

[30] M.M. Baig, M.A. Yousuf, M.F. Warsi, P.O. Agboola, M. Sher, I. Shakir, Surfactant assisted synthesis of rare earth Dy3+ substituted MnFe2O4 nanoparticles, Ceram Int. 45 (2019) 18014–18022. https://doi.org/10.1016/j.ceramint.2019.06.020.

[31] P. Anjana, R.S.A. Raj, R. Jose, M. Kumari, P.M. Sarun, D. Sajan, L.K. Joy, Highly enhanced dielectric permittivity in CoFe2O4 by the Gd substitution in the octahedral sites, J Alloys Compd. 854 (2021) 155758. https://doi.org/10.1016/j.jallcom.2020.155758.

[32] C. Murugesan, B. Sathyamoorthy, G. Chandrasekaran, Structural, dielectric and magnetic properties of Gd substituted manganese ferrite nanoparticles, Phys Scr. 90 (2015) 085809. https://doi.org/10.1088/0031-8949/90/8/085809.

[33] A.E. Danks, S.R. Hall, Z. Schnepp, The evolution of 'sol–gel' chemistry as a technique for materials synthesis, Mater Horiz. 3 (2016) 91–112. https://doi.org/10.1039/C5MH00260E.

[34] S. Thiagarajan, A. Sanmugam, D. Vikraman, Facile Methodology of Sol-Gel Synthesis for Metal Oxide Nanostructures, in: Recent Applications in Sol-Gel Synthesis, InTech, 2017. https://doi.org/10.5772/intechopen.68708.

[35] B.D. CULLITY, Elements of X-RAY DIFFRACTION, Addison Wesley, 1978.

[36] N. Perez, Crystallography, in: Phase Transformation in Metals, Springer International Publishing, Cham, 2020: pp. 1–44. https://doi.org/10.1007/978-3-030-49168-0_1.

[37] Experimental Crystal Structure Determination, Physics Tutorial, (n.d.). https://www.tutorsglobe.com/homework-help/physics/experimental-crystal-structure-determination-75516.aspx (accessed August 29, 2022).

[38] Powder X-ray Diffraction, (n.d.). https://chem.libretexts.org/Bookshelves/Analytical_Chemistry/Supplemental_Modules_%28Analytical_Chemistry%29/Instrumental_Analysis/Diffraction_Scattering_Techniques/Powder_X-ray_Diffraction (accessed August 29, 2022).

[39] K.G. Suastika, L. Yuwana, L. Hakim, Darmaji, D. Khusnul, Characterization of Central Kalimantan's Amethysts by Using X-Ray Diffraction, J Phys Conf Ser. 846 (2017) 012024. https://doi.org/10.1088/1742-6596/846/1/012024.

[40] G. Will, Powder Diffraction: The Rietveld method and the Two Stage Method to Determine and Refine Crystal Structure from Powder Diffraction Data, Physica-Verlag, 2006.

[41] R.A. Young, The Rietveld Method, Oxford University Press, 1995.

[42] M.S. Braga, O.F. Gomes, R.F.V.V. Jaimes, E.R. Braga, W. Borysow, W.J. Salcedo, Multispectral colorimetric portable system for detecting metal ions in liquid media, in: 2019 4th International Symposium on Instrumentation Systems, Circuits and Transducers (INSCIT), IEEE, 2019: pp. 1–6. https://doi.org/10.1109/INSCIT.2019.8868861.

[43] Tauc plot, (n.d.). https://en.wikipedia.org/wiki/Tauc_plot (accessed August 29, 2022).

[44] M. Dahim, R. Ismail, H. Al-Mattarneh, R. Hatamleh, Determination of leachate pollution content in soil using in-situ dielectric measurement, Adv Mater Lett. 10 (2019) 298–301. https://doi.org/10.5185/amlett.2019.2253.

[45] E. Barsoukov, Impedance Spectroscopy, Wiley, 2005. https://doi.org/10.1002/0471716243.

[46] A. Sinha, A. Dutta, Structural, optical, and electrical transport properties of some rare-earth-doped nickel ferrites: A study on effect of ionic radii of dopants, Journal of Physics and Chemistry of Solids. 145 (2020) 109534. https://doi.org/10.1016/j.jpcs.2020.109534.

[47] K.V. Zipare, S.S. Bandgar, G.S. Shahane, Effect of Dy-substitution on structural and magnetic properties of Mn Zn ferrite nanoparticles, Journal of Rare Earths. 36 (2018) 86–94. https://doi.org/10.1016/j.jre.2017.06.011.

[48] K.A. Mohammed, A.D. Al-Rawas, A.M. Gismelseed, A. Sellai, H.M. Widatallah, A. Yousif, M.E. Elzain, M. Shongwe, Infrared and structural studies of Mg1–xZnxFe2O4 ferrites, Physica B Condens Matter. 407 (2012) 795–804. https://doi.org/10.1016/j.physb.2011.12.097.

[49] S.B. Somvanshi, S.A. Jadhav, M. v. Khedkar, P.B. Kharat, S.D. More, K.M. Jadhav, Structural, thermal, spectral, optical and surface analysis of rare earth metal ion (Gd3+) doped mixed Zn–Mg nano-spinel ferrites, Ceram Int. 46 (2020) 13170–13179. https://doi.org/10.1016/j.ceramint.2020.02.091.

[50] A. Anwar, S. Zulfiqar, M.A. Yousuf, S.A. Ragab, M.A. Khan, I. Shakir, M.F. Warsi, Impact of rare earth Dy+3 cations on the various parameters of nanocrystalline nickel spinel ferrite, Journal of Materials Research and Technology. 9 (2020) 5313–5325. https://doi.org/10.1016/j.jmrt.2020.03.057.

[51] S.B. Somvanshi, S.A. Jadhav, M. v. Khedkar, P.B. Kharat, S.D. More, K.M. Jadhav, Structural, thermal, spectral, optical and surface analysis of rare earth metal ion (Gd3+) doped mixed Zn–Mg nano-spinel ferrites, Ceram Int. 46 (2020) 13170–13179. https://doi.org/10.1016/j.ceramint.2020.02.091.

[52] N.A. Bakr, S.A. Salman, H.F. Khudhair, Structural and Optical Properties of Zinc Doped Nickel Ferrite Ni(1-x)Zn(x)Fe2O4 Thin Films Prepared by Chemical Spray Pyrolysis Method, Journal of Chemical, Biological and Physical Sciences . 6 (2016) 280–293.

[53] P.R. Jubu, F.K. Yam, V.M. Igba, K.P. Beh, Tauc-plot scale and extrapolation effect on bandgap estimation from UV–vis–NIR data – A case study of β-

Ga2O3, J Solid State Chem. 290 (2020) 121576. https://doi.org/10.1016/j.jssc.2020.121576.

[54] V.R. Akshay, B. Arun, G. Mandal, M. Vasundhara, Visible range optical absorption, Urbach energy estimation and paramagnetic response in Cr-doped TiO $_2$ nanocrystals derived by a sol–gel method, Physical Chemistry Chemical Physics. 21 (2019) 12991–13004. https://doi.org/10.1039/C9CP01351B.

[55] H. Lemziouka, A. Boutahar, R. Moubah, L.H. Omari, S. Bahhar, M. Abid, H. Lassri, Synthesis, structural, optical and dispersion parameters of La-doped spinel zinc ferrites ZnFe2-xLaxO4 (x = 0.00, 0.001, 0.005, 0.01 and 0.015), Vacuum. 182 (2020) 109780. https://doi.org/10.1016/j.vacuum.2020.109780.